Medical Imaging with Laser Polarized Noble Gases

Timothy Chupp and Scott Swanson
University of Michigan
Departments of Physics and Radiology

January 28, 2000

Contents

Abstract

The field of medical imaging with polarized rare gases, just five years old, has brought optical scientists together with medical researchers to perfect techniques and pursue new opportunities for biomedical research. This review, written for the likely reader of these volumes, aims to present the field from several perspectives. The historical perspective shows how applications of nuclear polarization for experiments in nuclear and particle physics led to techniques for production of large quantities of highly polarized ^{3}He that are increasingly reliable and economical. The atomic/optical physics perspective details the underlying processes of optical pumping, polarization, and relaxation of the rare gases. The biomedical perspective describes work to date and the potential applications of imaging in medicine and research.

1 Introduction

Five years ago, a short article was published in the journal **Nature** showing Magnetic Resonance Images of ^{129}Xe gas that had filled the airways of an excised mouse lung [Albert et al., 1994]. The images were acquired at SUNY, Stony Brook, on Long Island, NY. But the gas, prepared by laser optical pumping methods, in Princeton, New Jersey, was transported over 100 km by car in a small glass cell immersed in a cup of liquid nitrogen. (The gas was "polarized" in Princeton to provide 10,000 times greater NMR signal per atom than produced by "brute force." This compensated for the 10,000 times lower concentration of gas.) Reading the Nature paper led many in the field of laser optical pumping to turn their attention to the new possibilities, and it led many radiologists to seek laser physicists as collaborators to help develop the potential biomedical applications. Now physicists, radiologists, neuroscientists, medical researchers, and clinicians are working together in teams around the world. The promise of entirely new ways to use NMR and MRI information from ^{3}He and ^{129}Xe images of gas in the lungs and of xenon dissolved in tissue of the lungs, heart, and brain, has attracted the attention of scientists, and physicians, as well as the pharmaceutical industry. The promise is that this marriage of laser/optical physics and medical imaging will provided new ways to study and map function in the brain, measure physiological parameters, and diagnose diseases of the lungs, heart, and brain that depend on the flow of gas and blood through the vital organs.

In figures 1,and 2, we show magnetic resonance images produced with laser polarized ^{3}He and ^{129}Xe. In figure 1, a series of consecutive images of a slice through the human lung shows the flow of gas into the air spaces after a breath is taken and exhaled [Saam et al., 1999]. This moving picture of gas flow is called a ventilation image. Ventilation images made with scintigraphy of radioactive gas (usually ^{133}Xe) are used to assess lung function and find non–functioning portions of the lung. Combined with measures of blood flow through the lung, ventilation scans help diagnose a variety of lung diseases, such as pulmonary embolism, with moderate specificity. (The efficacy of a diagnostic technique is characterized by its sensitivity and specificity. Sensitivity is essential to discover a malady
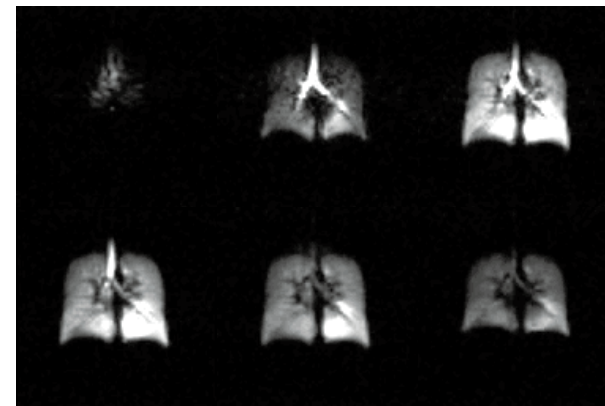

Figure 1: A ^{3}He ventilation image: a series of images taken at 0.8 second intervals after a breath of laser polarized ^{3}He is inhaled while the human subject is in the MRI scanner. The gas starts in the trachea, then moves out and down to the lower parts of the lung. The last frame shows the beginning of exhalation as the upward motion of the diaphragm expels gas from the lungs. *Images courtesy of Brian Saam. Used with permission.*

while specificity is required to determine the exact problem and the course of treatment.) In figure 2, we show images of ^{129}Xe gas in the lung and dissolved in tissue and blood of a rat that had been breathing a polarized ^{129}Xe – oxygen mixture. In contrast to helium, xenon crosses the blood–gas barrier in the lungs, dissolves in blood, and is carried to distal organs where it diffuses into tissue as the blood flows through capillaries from artery to vein. The NMR frequencies of ^{129}Xe differ by about 200 ppm for gas and dissolved phases, and vary by several ppm among different types of tissue and blood.

The development of techniques of laser enhanced nuclear polarization (or hyperpolarization), has been most strongly motivated by nuclear and particle physics. Targets of polarized ^{3}He are used in accelerator experiments such as those that probe the elementary particle, short range structure of the neutron [Chupp et al., 1994a]. Polarized ^{3}He is also used to polarize neutrons for nuclear physics and neutron scattering research [Coulter et al., 1988]. These driving motivations and applications
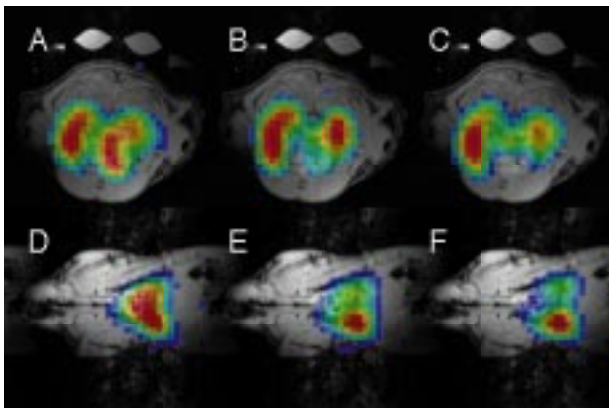
Figure 2: Magnetic Resonance Images of ^{129}Xe in the lungs and dissolved in the blood and tissue of a rat. The gray–scale images are conventional proton MRI (spin–echo) images that show the animal's anatomy. The false–color images show the concentration of ^{129}Xe magnetization for each of three spectral features corresponding to xenon in the gas phase (C and F), dissolved in tissue (B and E) and dissolved in blood (A and D). Panels (A through C) are called axial images across the body, and (D through F) are coronal images through the body.

along with other historical developments are described in section 1.1. The requirements of these experiments have pushed us to understand the physics and technical limitations of optical pumping at high densities. Now, we can produce liters (at STP) of ^{3}He, polarized to 50% or more, and similar quantities of ^{129}Xe. Optical pumping, polarization techniques, lasers, and other technical details are discussed in section 2, and the basics of NMR and MRI are described in section 3. The exciting new possible applications to medical imaging are described in sections 4 and 5 on air space imaging and dissolved phase imaging respectively. We conclude in section 6 emphasizing some of the potential applications and future promise of this new technique that provides a wonderful example of transfer of technology motivated by fundamental physics research.

1.1   Historical perspective

The atomic nucleus of an odd-A or odd-Z isotope in general has non–zero nuclear spin and non-zero magnetic moment. These nuclear spins and moments have long been important in the development of nuclear physics through the comparison of experiment with the nuclear shell model theory (see for example, Ramsey's book on Nuclear Moments [Ramsey, 1953]). Nuclear spin has also been an important variable for a range of approaches to studying nuclear interactions. Perhaps the best example is ^{3}He. The stable $A = 3$ isotope, ^{3}He, has been extremely important in nuclear physics. Calculation of the magnetic moment has clarified the role of meson exchange corrections. Nuclear reactions induced by ^{3}He and ^{3}H allow study of isospin symmetry and isospin dependence in a unique way because the A=1 isodoublet is much more difficult experimentally – accelerated neutron beams are not feasible. Perhaps most important is the fact that the neutron polarization in a polarized ^{3}He nucleus is $\approx 87\%$. This has allowed important short range properties of the neutron to be measured including the neutron electric charge distribution – the electric form factor G_E^n – and the neutron deep inelastic scattering spin structure functions $g_n(x)$. Therefore beams and targets of polarized ^{3}He have been sought since at least the 1950's. It was the late 1980's before the basic physical processes and technology came together to foresee practical polarized ^{3}He targets.

^{3}He was accidently discovered by Alvarez at the Berkeley cyclotron in a test run preliminary to the intended use of the Cyclotron as a mass spectrometer to detect ^{3}He produced in nuclear reactions [Alvarez, 1987]. (It had been assumed, following the suggestion of Hans Bethe, that ^{3}He was unstable.) After the experiment, the magnet was ramped down with the RF on, revealing an ion with $Z/A = 2/3$. Once the Cyclotron magnet was shimmed properly for this mass, the discovery of ^{3}He was confirmed. One surprising consequence of that discovery was that ^{3}He and not ^{3}H is the stable A=3 isotope. With two protons and one neutron, the ^{3}He nucleus must have half integer spin, and naive consideration of the Pauli principle suggests that the protons' spins pair in a singlet $l = 0$ state. In that case the entire angular momentum and magnetic moment of the ^{3}He nucleus would be due to the neutron. In fact ^{3}He as well as ^{3}H are spin 1/2, but the tensor component of the nuclear force and isospin breaking lead to a complicated many component wave function with $l = 0, 1$ and 2, and mixed isospin states [Afnan and Birrell, 1977]. The total angular momentum of the nucleus has contributions from the D–state and a small proton polarization opposite the ^{3}He polarization. Even this is not enough to account for the measured magnetic moments: isovector meson exchange currents apparently contribute opposite amounts to the ^{3}He and ^{3}H magnetic moments. Therefore the total magnetic moment of ^{3}He can be written

$$\mu_z(^3\text{He}) = P^n \mu_n + P^p \mu_p + \mu_N(<L_z> + A_{MEC} <I_z>) \tag{1}$$

where $P^n = 2 <s_z^n> = 0.87$ and $P^p = -0.027$ are respectively [Friar et al., 1990] the neutron and proton polarizations, $<L_z> = 0.061$. The meson exchange correction is $A_{MEC} <I_z> = -0.35$ for the isospin projection $I_z = -1/2$. The nuclear magneton is $\mu_N = e\hbar/2m_pc$.

^{3}He is rare, and this is a problem. Primordial abundance of ^{3}He produced in Big Bang nucle-

osynthesis is [^{3}He]/[^{4}He]=0.00004 [Arnett and Turan, 1985]. Additional ^{3}He has been produced in stellar burning [Trimble, 1982], in the atmosphere due to cosmic ray interactions, and underground due to natural radioactivity. Cosmic ray production of ^{3}He on the moon, which does not have atmospheric shielding from cosmic rays, has left much greater abundances imbedded in lunar rocks [Wittenberg et al., 1986], though mining the moon may remain impractically expensive. Most of the stored ^{3}He reserve, less than 1000 kg, has come from the decay of tritium (^{3}H) produced for thermonuclear weapons.

Another feature of ^{3}He has motivated work to develop polarization techniques. ^{3}He turns out to be a potentially perfect spin filter for polarization of neutrons. The strong neutron absorption reaction n+^{3}He → p + ^{3}H is nearly 100% polarization dependent, due to an unbound $J = 0$ resonance in ^{4}He. With the neutron and ^{3}He spins opposite, the absorption cross section is $\sigma_a(v) = 5230 \frac{v_0}{v}$ barns (v_0 =2200 m/s is the *rms* velocity of thermal neutrons). Other n+^{3}He interactions are negligible. Passing a neutron beam through a filter of polarized ^{3}He produces a beam polarized parallel to the ^{3}He, though reduced in flux [Williams, 1980, Coulter et al., 1988, Coulter et al., 1990]. The polarization and transmission for a filter with ^{3}He thickness [^{3}He]t and polarization P_3 are given by

$$P_n = \tanh(\sigma_a[^3\text{He}]tP_3) \quad P_t = \cosh(\sigma_a[^3\text{He}]t)P_3\exp(\sigma_a[^3\text{He}]tP_3) \qquad (2)$$

Polarized neutron beams are widely sought for condensed matter and materials science research [Fitzsimmons and Sass, 1989] and for studies of the nuclear interactions of scattered [Heckel et al., 1982], absorbed [Mitchell et al., 1999], and decaying neutrons [Abele et al., 1997]. Scattering of neutrons from materials reveals structure and momentum distributions, and the spin dependence is used to study magnetism, for example of multiple thin layers sought for magnetic recording media [Kubler, 1981]. In contrast to synchrotron x–rays, the magnetic interactions of neutrons are comparable in strength to electric interactions; for photons, magnetic interactions are suppressed by $\approx$ 300. The decay of polarized neutrons provides the opportunity to study the weak interactions [Jackson et al., 1957], and weaker interactions [Herczeg, 1998] such as those that emerge from extensions of the Standard Model of elementary particle interactions including SuperSymmetry.

The first attempts to produce useable polarized ^{3}He targets were not successful in spite of heroic efforts. Most notable was the effort by Daniels and Timsit [Timsit et al., 1971a, Timsit et al., 1971b]. Employing optical pumping of metastable helium atoms with lamps (described in section 2), they developed a mercury Toeppler pump (later adapted by Heil and co–workers [Becker et al., 1994]) and provided an important study of ^{3}He polarization relaxation in the presence of many materials [Timsit et al., 1971b]. One particularly crucial conclusion was the importance of a predominantly glass system. Timsit and Daniels presented a theory for predicting ^{3}He polarization relaxation rate dependence on helium permeability and glass iron content that confirmed that one should use alumino–silicate glasses such as Corning 1720 [Fitzsimmons et al., 1969], Schott Supermax [Becker et al., 1994], and Corning 7056 [Smith, 1998], . Quartz and fused silica, though relatively porous to helium, can be produced with extremely low iron content, and are useful particularly for neutron spin filters since the

^{10}B in most glasses strongly absorbs low energy neutrons. Timsit's and Daniel's efforts fell short of the goals of 0.5 liter-atm of ^{3}He with 25% polarization. A decade later, the availability of lasers led to success with the first ^{3}He neutron spin filter [Coulter et al., 1990] and the first targets for electron scattering for study of the neutron charge form factor G_E^n by quasielastic scattering of polarized electrons from the polarized ^{3}He [Woodward et al., 1990, Thompson et al., 1992, Chupp et al., 1992, Becker et al., 1994]. (Quasielastic scattering breaks up the nucleus by momentum transfer to a single nucleon. The spin dependence is generally dominated by the neutron.)

The next generation of polarized ^{3}He target was used for electron scattering at SLAC in a program that revealed the spin content of the neutron's quarks in deep inelastic scattering [Anthony et al., 1993, Middleton et al., 1993, Abe et al., 1997]. These targets employed spin exchange with laser polarized Rb vapor, a technique that had been considered less favorable for several reasons including the extremely weak hyperfine spin exchange interaction [Walker and Happer, 1997] and problems of radiation trapping – depolarization by multiple scattering of photons in the dense alkali–metal vapor. However, it had been shown that 60-100 torr of N_2 is sufficient to suppress radiation trapping [Hrycyshyn and Krause, 1970] and that optical pumping with lasers was effective at extremely high optical density with [Rb]$\approx 10^{15}$ cm^{-3} [Chupp and Coulter, 1985]. More detailed studies of optical pumping at high alkali–metal density [Chupp et al., 1987, Wagshul and Chupp, 1994] showed that laser *intensity* was the primary limitation and that ^{3}He pressures greater than 10 bar in volumes limited only by laser power to 200 cm^3 became possible with CW standing wave Titanium::sapphire lasers [Larson and *et al.*, 1991].

The two methods for polarizing ^{3}He, discovered in the early 1960s, became competing techniques in the 1980s. Metastability exchange was pursued by Leduc, Schaerrer and co–workers who teamed up with Otten and Heil at Mainz [Becker et al., 1994] and with Woodward, McKeown and Milner [Bohler et al., 1988]. This led to the neutron spin filter program at ILL, Grenoble [Surkau et al., 1997, Heil et al., 1998], and quasielastic scattering measurements at Mainz [Becker et al., 1994, Becker et al., 1998], both using a two stage, titanium pump compressor to increase the ^{3}He pressure from 1 torr to $\approx$ 1 bar. The metastability exchange technique has also been used to pump ^{3}He into a cooled cell in a quasielastic scattering experiment [Woodward et al., 1990] and to fill a "storage cell" that is coaxial with the circulating 30 GeV positron beam in the HERA ring at DESY, Hamburg, Germany [Ackerstaff et al., 1997]. Spin exchange has been most successful in producing high density polarized ^{3}He that is essential for targets used in extracted beam experiments such as the SLAC End Station A deep inelastic scattering program [Abe et al., 1997, Anthony et al., 1996] and recent efforts at TJNAF in Newport News, Virginia [Gao, 1998].

The possibility of nuclear spin gyroscopes also emerged as optical pumping techniques were developed[Colgro Grover, 1983]. A nuclear spin gyroscope does not require the large quantities of highly polarized ^{3}He demanded by applications of polarized nuclear targets and polarized neutrons. However the concept does rely on the longest possible spin–relaxation and spin–coherence times. Long spin–relaxation times are also important for high polarization, and the development of gyroscopes at industry labs

helped advance the study of surface relaxation mechanisms.

While the technical advances in polarized ^{3}He have been largely motivated by work on polarized targets for nuclear and high energy physics, ^{129}Xe polarization was advanced in the optical pumping studies led by Happer and co–workers [Zeng et al., 1985]. Early in the 1980s they began extensive investigations of spin exchange between noble gases and optically pumped alkali-metal vapors [Happer et al., 1984]. They studied many processes involved in optical pumping of alkali–metal vapors in the presence of buffer gases providing extensive data on the xenon–Rb system [Zeng et al., 1985]. ^{129}Xe polarization of nearly 100% in small $\approx$ cm^3 volumes was produced, Experiments included studies of $I = 3/2$ ^{131}Xe as well as a radioactive isotopes (^{131}Xe^m, ^{133}Xe and ^{133}Xe^m) [Calaprice et al., 1985]. The work of Cates and Happer, with co–workers[Cates et al., 1990, Gatzke et al., 1993], on polarized frozen ^{129}Xe as a means for accumulating large quantities of polarized gas, may have been the initial inspiration for the development of MRI with laser polarized xenon. The first experiment at Stony Brook with gas polarized in Princeton relied on freezing the xenon for transport by car. The magnetization lifetime of frozen^{129}Xe is generally much longer than in the gas phase[Gatzke et al., 1993].

Studies of spin exchange between Rb and lighter noble gases ^{21}Ne [Grover, 1983] and ^{3}He [Chupp and Coulter, 1985, Chupp et al., 1987] were motivated by nuclear physics applications, in particular the use of symmetry violations such as Parity (P) and Time Reversal (T) to study weak interactions in the presence of the dominant strong and electromagnetic interactions [Chupp et al., 1988]. Several experiments used $I = 3/2$ ^{21}Ne and ^{3}He simultaneously to search for quadrupolar interactions such as a possible dependence of nuclear binding energy on orientation with respect to an assumed absolute rest frame of the Universe [Chupp et al., 1989]. These pulsed NMR experiments were probably the first applications that specifically used laser polarized rare gases to enhance rare gas NMR signals by many orders of magnitude.

A variety of experimenters have since used laser polarized ^{3}He and other noble gases to enhance NMR measurements. The low temperature work at Ecole Normal Superieur has used NMR to measure polarization and probe such phenomena as spin waves [Tastevin et al., 1985] and the properties of fermi liquids [Leduc et al., 1987], and ^{3}He–^{4}He mixtures [Himbert et al., 1989, Nacher and Stolz, 1995]. Geometric phases have been measured with ^{129}Xe [Appelt et al., 1995]. Measurement of the NMR splittings of ^{129}Xe and ^{3}He in the presence of an electric field is used to search for T–violation [Rosenberry, 1999]. This experiment used a Spin Exchange Pumped Zeeman Maser [Chupp et al., 1994b, Stoner et al., 1996] that exploits cavity–spin coupling and the population inversion pumped into the nuclear spins [Robinson and Myint, 1964, Richards et al., 1988].

Conventional NMR research with ^{129}Xe (*i.e.* not laser enhanced) has focused on variety of problems including cross polarization, molecular dynamics, xenon molecules (*e.g.* XeF$_5$), diffusion in porous media, polymers, and liquid crystals. ^{131}Xe has been used to study quadrupolar relaxation on surfaces, in macromolecules, and porous media. Xenon has been extremely important because it is normally gaseous, can be easily frozen or liquified, is relatively soluble, and is characterized by large NMR chemical shifts up to 500 ppm between the gas and dissolved phases. Alex Pines and his group

recognized that many of these applications of NMR research could be enhanced with laser polarized ^{129}Xe [Raftery et al., 1991], and inspired the original pursuit of MRI with laser polarized noble gases [Song et al., 1999].

2 Nuclear Polarization Techniques

Polarization of ^{3}He and ^{129}Xe can be contemplated by brute–force, Stern–Gerlach, or by optical–pumping techniques. Brute–force polarization uses high magnetic fields and low temperatures to create an imbalance of nuclear spin state populations. At low temperatures ^{3}He atoms in the liquid phase are indistinguishable obeying Fermi-Dirac statistics with the consequence that negligible polarization can be achieved at reasonable magnetic fields. (The effective spin temperature does not drop below the Fermi Temperature of $T_F = 0.18K$.) For solid ^{3}He, the lattice positions, not the momentum states, distinguish atoms, and Boltzmann statistics describe the polarization. The result is that solid ^{3}He can be polarized, achieving the equilibrium value

$$P_3 \approx \tanh(\mu B/kT), \qquad (3)$$

which at 10 mK and 10 T gives $P_3 = 91.5\%$. Low temperature alone is not sufficient to produce solid ^{3}He – high pressures are also needed. The Pomeranchuk method involves cooling the liquid in an applied magnetic field under pressure. For $T < 0.32$ K, the liquid's entropy is less than the solid's and the sample cools itself in a process similar to cooling by evaporation [Lounasmaa, 1974]. Using this method to polarize, followed by rapid warming of the polarized ^{3}He through the liquid phase, Forassatti [Frossati, 1998] has proposed producing a thousand liters of highly polarized ^{3}He per day. It is not known whether ^{129}Xe can be polarized in this way, though measured spin diffusion times seems favorable.

Stern Gerlach techniques have been used to produce beams of highly polarized ^{3}He. However the tradeoffs of acceptance and polarization have limited fluxes to $\approx 10^{14}$/s with $P_3 = 0.9$ for a hexapole magnet. This is not sufficient for accumulation of useful quantities, though it is useful for applications where a trace amount of highly polarized ^{3}He is required [Golub and Lamoreaux, 1994].

Optical polarization employing either hyperfine spin exchange with an alkali-metal vapor [Bouchiat et al., 19 for ^{3}He and ^{129}Xe or optical pumping of metastable helium atoms, for ^{3}He [Colgrove et al., 1963] emerged as promising techniques with the availability of lasers. Both techniques are now used to produce liter quantities (at STP) with polarization $P_3 > 50\%$ that are used for neutron polarization, polarized targets, and for medical imaging.

In all cases, relaxation of nuclear spin must be balanced by polarization rates. (Note that nuclear spin relaxation in a biological environment *in vivo* or *in vitro* is completely different from relaxation in a carefully prepared polarization system as discussed in sections 4 and 5.) Rare gas nuclear spin relaxation occurs by bulk collisions with impurities, dipole–dipole interactions in the bulk, magnetic field

gradients, and surface wall interactions. The most important impurity is paramagnetic O_2. Relaxation rates are proportional to the oxygen impurity level with rate constants $k(O_2\text{-}^{129}\text{Xe}) \approx 0.3/\text{s}^{-1}/\text{amagat}$ [Jameson et al., 1988] and $k(O_2\text{-}^3\text{He}) \approx 0.45 \text{ s}^{-1}/\text{amagat}$ [Saam et al., 1996] at 14.1 kG and at room temperature with temperature dependence $\approx T^{-1/2}$. (One amagat is the number density of a gas at STP). In order to achieve high ^{3}He polarizations, O_2 impurity levels must be below parts per million. Relaxation due to dipole–dipole interactions have rate constants $k(^{129}\text{Xe-}^{129}\text{Xe})=5 \times 10^{-6}/\text{s}/\text{amagat}$ [Hunt and Carr, 1963] and $k(^3\text{He-}^3\text{He})=4\times10^{-7}/\text{s}/\text{amagat}$ [Mullin et al., 1990, Newbury et al., 1993]. Magnetic field gradient contributions to nuclear spin relaxation arise due to non–adiabatic evolution of the nuclear spin as the atoms move in the gradients between collisions. For the high densities encountered in most applications

$$\Gamma_{\Delta B} \approx D \frac{|\nabla B_x|^2 + |\nabla B_y|^2}{B^2} \qquad (4)$$

Typically, magnetic field gradients of 0.3-1%/cm are sufficient for ^{3}He and ^{129}Xe polarization respectively. Wall interactions are moderately well understood. For ^{3}He, the work of Timsit and Daniels described above shows that paramagnetic impurities and sticking time, dominated by diffusion of helium into the surface, are most important. Coating the surfaces of glass or fused silica with cesium has proved effective for attaining ^{3}He relaxation times of 2 days or more [Cheron et al., 1995, Surkau et al., 1997]. For highly polarizable xenon atoms, the sticking times are much shorter, but relaxation rates can be reduced with silane wall coatings [Zeng et al., 1985, Oteiza, 1992, Sauer et al., 1999]. Sauer has shown evidence that ^{129}Xe–proton dipolar interactions dominate relaxation in coated cells. With coatings, relaxation times for ^{129}Xe of ten minutes or more are common at low magnetic fields. At 2T, $T_1 > 2$ hours has been observed for ^{129}Xe indicating decoupling of the wall relaxation mechanisms.

2.1   Optical Pumping and Spin Exchange

Optical pumping [Kastler, 1950] is the means by which the internal degrees of freedom of a sample of atoms can be manipulated with light, and the angular momentum of the photons can be transferred with high efficiency to the atoms (see [Happer, 1972]). The most effective way to understand optical pumping and spin exchange is by derivation of rate equations describing these processes. For optical pumping, we begin by considering an atom with $J = 1/2$, such as an alkali-metal atom with nuclear spin $I = 0$. The polarization, P, is given by

$$P = \rho_{\frac{1}{2}\frac{1}{2}} - \rho_{-\frac{1}{2}-\frac{1}{2}} \quad \text{and} \quad \rho_{\frac{1}{2}\frac{1}{2}} + \rho_{-\frac{1}{2}-\frac{1}{2}} = 1 \ . \qquad (5)$$

Both polarization and spin destruction processes must be considered. For polarization, we assume that the atoms are illuminated with right circularly polarized (σ_+) light, and we define the total the

rate **per atom** of pumping out of the $m_j = -1/2$ state and into the $m_j = +1/2$ state as $\gamma_{opt}\rho(-1/2)$. For atoms with resonant frequency ν_0

$$\gamma_{opt}(\vec{r}) = k \int d\nu \ \Phi(\vec{r}, \nu)\sigma(\nu - \nu_0). \qquad (6)$$

The laser intensity per unit frequency is $\Phi(\vec{r}, \nu) = dI(\vec{r})/d\nu$, which is in general position dependent. The cross section for absorption of *unpolarized* light is $\sigma(\nu)$, and k is a constant that accounts for the relative probability that an atom, after absorbing a photon, also absorbs its angular momentum. For alkali–metal atoms in the presence of sufficient buffer gas pressure to collisionally mix and randomize the spin projections in the p states, $k = 1$.

The optical pumping rate equations for the two state system are

$$\frac{d\rho(\pm 1/2)}{dt} = \pm \left[\frac{\Gamma_{\text{SD}}}{2} + \gamma_{opt}\right] \rho(-1/2) \mp \frac{\Gamma_{\text{SD}}}{2}\rho(+1/2). \qquad (7)$$

We have included possible relaxation of electron spin polarization in the term Γ_{SD}.

For spin exchange pumped ^{3}He, Rb spin relaxation is dominated by collisions with Rb atoms, ^{3}He and N_2 and to a lesser degree by wall interactions [Wagshul and Chupp, 1994]. Walker has recently discovered a surprising magnetic field dependence to the Rb-Rb relaxation process that decouples at relatively low fields of a few hundred Gauss [Kadlecek et al., 1998]. This suggests a time scale much longer than characteristic of binary collisions between Rb atoms. Though the mechanism is not yet understood, it is clear that optical pumping at magnetic fields of a few kG can turn off the Rb-Rb collisions with the advantages of potentially higher Rb polarization or less laser power. Rb-Rb collisions are generally less important than Rb–^{3}He or Rb–^{129}Xe collisions. For ^{3}He polarization, it is most effective to use high ^{3}He density so that Rb-^{3}He collisions dominate the Rb spin destruction rate. For ^{129}Xe, spin destruction is so strong that the same is effectively true, though xenon densities are much lower. Therefore the laser intensity requirements are determined by the Rb-noble gas spin destruction rate Γ_{SD}.

There are good spin destruction collisions, and there are bad ones. A good one, of course, results in a spin exchange to the noble gas nucleus. In a bad collision, the Rb atom looses its electron spin polarization to rotational angular momentum. It turns out that the ratio of spin exchange to spin rotation varies significantly among the alkali–metal atoms. Rb is worse than K, by nearly an order of magnitude, though the spin exchange rate constants are apparently approximately equal [Romalis et al., 1998]. This has become very important recently with the availability of high powered LDAs at 770 nm, the D1 wavelength for K. As long as it is practical to operate at temperatures of $250°$ C at which the density of K is sufficient for spin exchange to balance ^{3}He relaxation, we can expect increased use of K as the spin exchange partner.

Radiation trapping is also a potential limitation to optical pumping in polarized targets [Holstein, 1947]. This occurs when the mean free path for the unpolarized photons is much less than the dimensions of

the pumping vessel. The incident σ_+ photons can be reemited (*i.e.* resonantly scattered) and depolarized. Each unpolarized photon can multiply scatter and depolarize many atoms and therefore radiation trapping can be thought of as an additional relaxation mechanism that is a function of incident laser power. Radiation trapping would limit the density of the mediating alkali-metal species in spin exchange pumped ^{3}He targets. However molecular N$_2$ [Zeng et al., 1985, Chupp and Coulter, 1985] (for ^{3}He) have been shown to effectively mitigate radiation trapping effects. At high magnetic field the Zeeman splitting of the $S_{1/2}$ and $P_{1/2}$ states causes the scattered photons to be off resonance and only very weakly absorbed in depolarizing transitions. The presence of N$_2$ or other molecular species quenches the $P_{1/2}$ states non-radiatively reducing the branching ratio for radiative decay (i.e. resonant scattering) [Wagshul and Chupp, 1989].

Assuming that the complication of radiation trapping has been practically eliminated, the steady state solution to the rate equations predicts electron spin polarization

$$P_S = \frac{\gamma_{opt}(\vec{r})}{\gamma_{opt}(\vec{r}) + \Gamma_{SD}}. \tag{8}$$

and a time constant $(\gamma_{opt}(\vec{r}) + \Gamma_{SD})^{-1}$ that is typically milliseconds.

For atoms with nuclear spin, including alkali–metal atoms and metastable ^{3}He atoms, the hyperfine coupling results in total angular momentum F. Laser optical pumping must provide the angular momentum for complete atomic polarization, the time dependence becomes more complicated than the single exponentials that describe the two state system, the transients become longer, and the nuclear spin serves as a reservoir of angular momentum [Bhaskar et al., 1982, Nacher and Leduc, 1985, Wagshul and Chupp, 1994, Appelt et al., 1998]. However, the levels rapidly reach a spin temperature equilibrium mediated by electron spin exchange [Anderson and Ramsey, 1961] and it is sufficient to consider only the evolution of electron spin **S**. For the metastability exchange, the discharge itself also leads to relaxation.

The spin excahnge rate equations, including relaxation, can be written

$$P_I = \gamma_{SE}(P_S - P_I) - \Gamma P_I \tag{9}$$

where $P_I = 2 < I_z >$ (for $I = 1/2$) is the rare gas nuclear polarization and $P_S = 2 < S_z >$ is the alkali–metal electron polarization. The steady state solution is

$$P_I = P_S \frac{\gamma_{SE}}{\gamma_{SE} + \Gamma}. \tag{10}$$

The goal is therefore to maximize alkali–metal electron spin polarization and effect long relaxation times so that $\Gamma << \gamma_{SE}$.

For ^{3}He polarized by spin exchange with Rb, γ_{SE} is typically many hours and relaxation times of days have been achieved, resulting in high polarizations greater than 50%. Relaxation seems to be limited by many factors including wall relaxation, interactions with impurity gases (probably paramagnetic O$_2$), and dipolar relaxation in ^{3}He–^{3}He collisions.

For ^{129}Xe, $1/\gamma_{SE}$ is typically several minutes but can be as short as 10 seconds. Relaxation times in silane coated cells seem to be 10-30 minutes at low magentic fields, and several hours at 2T [Zeng et al., 1985, Oteiza, 1992]. Dueterated coatings have been suggested to reduce relaxation at low field [Sauer et al., 1999]. Relaxation is often dominated by wall collisions, though impurities and dipolar relaxation are also important.

In a collision between an alkali–metal atom with electron spin polarization and a rare gas atom with $I = 1/2$, the electron spin couples to the nuclear spin and to the rotational angular momentum of the pair [Happer et al., 1984]. The dominant contributions to the spin dependent hamiltonian are

$$H' = \gamma \mathbf{N} \cdot \mathbf{S} + A\mathbf{K} \cdot \mathbf{S} + A_{SE}\mathbf{K} \cdot \mathbf{S} \tag{11}$$

where A is the alkali-metal hyperfine interaction and A_{SE} is the spin exchange hyperfine interaction, both of which are in general position dependent. However the long range contributions vanish for spherically symmetric collisions, and only the Fermi–contact term acts, so that

$$A_{SE} = \frac{8\pi}{3} 2\mu_B 2\mu_I \delta^3(R). \tag{12}$$

Where $\delta^3(r - R) = |\psi(R)|^2$ is the probability that the alkali–metal valence electron (coordinate r) is at the position of the noble gas nucleus (coordinate R). Herman has shown that $|\psi(R)|^2$ is in fact enhanced due the electron exchange interactions as the electron is attracted by the positive charge of the nucleus [Herman, 1965]. An enhancement factor is defined in terms of the free alkali–metal electron wave function(ψ_0) by $|\psi(R)|^2 = |\eta\psi_0(R)|^2$. $|\eta|$ varies from about 10 for Rb-^{3}He to 50 for Rb-^{129}Xe [Walker, 1989].

The hyperfine interaction H' is, of course, time dependent as an alkali–metal atom and rare gas atom move past each other. For ^{3}He, the time scale is about 10^{-12} s because the collisions are always binary – in contrast to ^{129}Xe which can form a Van der Waals molecule with an alkali–metal atom in a three body collision [Bouchiat et al., 1972]. The lifetime of this molecule can be 10^{-9} s or longer, limited in fact by the break up of the molecule in a collision with another buffer gas molecule. One consequence is that the rate constants for spin exchange are much different for ^{3}He polarization and ^{129}Xe polarization: k_{SE}(Rb-^{3}He) = $6 - 12 \times 10^{-20}$ cm^3/s and k_{SE}(Rb-^{129}Xe $\geq 4 \times 10^{-16}$ cm^3/s, with this lower limit set by binary spin exchange in the absence of three body formation of Van der Waals molecules [Cates et al., 1992]. Spin rotation is a sink of angular momentum resulting from the coupling of the electron spin to the rotation of the alkali–metal–noble–gas pair, and is generally dominated by the heavier partner as discussed in [Walker and Happer, 1997].

If we neglect wall interactions, alkali–alkali collisions, and alkali–N$_2$ collisions, the alkali–metal electron spin destruction rate reduces to the sum of spin exchange and spin rotation:

$$\Gamma_S D > k_S E[I] + k_S R[I] \tag{13}$$

for a rare gas of number density $[I]$. Since the incident, circularly polarized laser photons must balance this spin destruction rate, it is useful to consider the spin exchange efficiency

$$\epsilon_{SE} = \frac{k_S E}{k_S E + k_S R}. \tag{14}$$

This quantity, in principle sets an upper limit on the "photon efficiency" (defined by [Bhaskar et al., 1982]) with which optical pumping can balance noble gas relaxation. In general, however, photon efficiency is much lower than ϵ_{SE} because of other alkali–metal spin destruction mechanisms, necessarily inefficient optical transport of laser light into the cell, and the fact that lasers used in practical situations are broad band (as discussed below). The magnetic field dependence of spin exchange, spin rotation, and relaxation mechanisms are, of course, important, particularly in magnetic imaging applications at fields of 2T and greater [Happer et al., 1984].

2.1.1 ^{3}He

Spin exchange cross sections for Rb-^{3}He have been estimated in [Walker, 1989] and measured by several groups. Measurements of ^{3}He nuclear spin relaxation rates in the presence of Rb [Bouchiat et al., 1960, Gamblin and Carver, 1965, Coulter et al., 1988, Cummings et al., 1995] show that $< \sigma_{SE}v >= 4 - 8 \times 10^{-18}$ cm^3/s. Measurement of the frequency shifts of ^{3}He NMR and Rb EPR frequencies are consistent with this range [Baranga et al., 1998]. The frequency shift measurements also allowed comparison of the Rb-^{3}He and K-^{3}He spin exchange interaction, showing that they are within 10% of each other. Since ^{3}He nuclear spin relaxation times are generally 10's of hours, polarization times must be only a few hours. This requires alkali-metal density greater than 10^{14}/cm^3. Since cell volumes are $\approx$100 cm^3, or greater, the total number of alkali-metal atoms can be $> 10^{17}$, the incident photon flux must balance the loss of angular momentum by the alkali-metal atoms. The dominant processes relevant to Rb-^{3}He spin exchange can be summarized by the Rb spin destruction rate [Wagshul and Chupp, 1994, Walker and Happer, 1997, Appelt et al., 1998]

$$\Gamma_{SD} = k_{Rb-^3He}[^3\text{He}] + k_{Rb-N_2}[\text{N}_2] + k_{Rb-Rb}[Rb] \tag{15}$$

where the $k's$ are rate constants for spin destruction due to collisions with each of the species in the optical pumping cell. For a typical application, $\Gamma_{SD} \approx 500$ Hz and 10^{18} photon/s/cm^3 or 100 mW/cm^3 are necessary.

2.1.2 ^{129}Xe

There are crucial distinctions for ^{129}Xe polarization: The xenon–alkali–metal spin exchange and spin rotation rate constants are many orders of magnitude larger than for helium [Cates et al., 1992], and long lived Van der Waals molecules, formed in 3-body collisions with lifetimes comparable to the hyperfine mixing time, may dominate spin exchange and spin–rotation. As a result, polarization rates have characteristic time constants in the range of 10 s to several minutes in practical situations [Zeng et al., 1985]. These times are comparable to and shorter than ^{129}Xe nuclear spin relaxation times in the polarization apparatus so the ^{129}Xe polarization is generally limited by the Rb or K polarization, not relaxation mechanisms, as in the case of ^{3}He. The situation can be quite different, however, in systems designed to collect xenon gas that has flowed through a polarization chamber, such as that developed by Dreihuys *et al.* [Driehuys et al., 1996]. In this case, the Rb density is probably not well controlled, and the xenon atoms may not uniformly sample the Rb polarization in the pumping chamber. This may be the reason that the observed ^{129}Xe polarization is generally much lower than the Rb polarization [Hasson et al., 1999b].

2.1.3 Lasers for Spin Exchange Pumping

Lasers have been the essential light source for successful polarized ^{3}He and ^{129}Xe experiments. Originally dye lasers were used, producing up to 1 watt near 795 nm with linewidths less than or comparable to the pressure broadened Rb absorption linewidth [Chupp et al., 1987]. (Typical standing wave dye laser linewidths are 30 GHz; the Rb D1 line is broadened by about 18 GHz per amagat of ^{3}He.) In the late 1980's, high powered arrays of laser diodes (LDAs) became available, and their suitability for spin exchange pumped ^{3}He polarization was of immediate interest [Wagshul and Chupp, 1989]. Simultaneously the Titanium::sapphire laser was developed for high power applications and soon became commercially available. By about 1990, the cost per useful watt of LDAs and Ti::sapphire lasers was comparable, but a single Ti:sapphire set up could produce 5 watts whereas the most powerful available LDA was 2 watts. Also, 795 nm was at the edge of reliable LDA production. Several experiments were undertaken each using one or more Ti:sapphire laser. Experiment E142 at SLAC ran with up to five [Middleton et al., 1993].

By 1994, bars of LDA's had become available with a price per watt of $500 and falling rapidly. This has been the single most important technology advance driving this field. By comparison, a Ti:sapphire laser pumped by a large frame Argon ion laser has a price per watt of $15K-$20K. Current LDA prices are $100-$200 per watt. LDA's will dominate future experiments and make polarized ^{3}He and ^{129}Xe much more widely accessible.

2.1.4 Optical Pumping with Laser Diode Arrays

Laser didoes are widely recognized as work horses in atomic and optical physics. For example, near IR lasers used in cooling and trapping of K, Rb, and Cs, are generally single mode (line widths on the order of MHz) and low powered (50-100 mW with 500 mW amplifiers commonly in use). High powered LDAs are produced for a variety of commercial, industrial, and communications applications (including stripping the paint from battle ships). Currently available LDA packages utilized for Rb optical pumping consist of bars of individual LDAs. Bars with 20-50 watt nominal output consisting

of about 20 1-3 watt elements with GaAlAs and InGaAsP can be purchased for a few thousand dollars each. The injection current and temperature of the device are used to tune the arrays to 794.7 nm, the Rb D1 wavelength, and typical bandwidth is 2-4 nm. Recently, 20 watt bars at 770 nm, the K D1 wavelength have become commercially available.

Though the broadband light from a LDA is spread over 1-2 nm, much greater than the 0.1-0.2 nm typical homogeneously broadened absorption line width of Rb, the convolution of the light intensity and the absorption cross section provides a sufficiently high photon absorption rate that light 1 nm or more off resonance can effectively polarize Rb. The photon absorption rate of laser light by Rb atoms is defined in equation 6. In the case of LDAs, $\Phi(\nu)$ is spread over 2 nm or more, as shown in figure 3. The total power output per laser is about 15 watts. As the light propagates through the cell (along z), it is absorbed by the Rb at a rate

$$\frac{d\Phi(\nu)}{dz} = -\sigma(\nu)[\text{S}]\Phi(z)(1 - P_\text{S}(z)) \quad \text{where} \quad P_\text{S} = \frac{\gamma_{opt}(z)}{\gamma_{opt}(z) + \Gamma_{SD}} \tag{16}$$

Computer modeling based on numerical integration of these equations is generally reported by several authors to predict results for ^{3}He and ^{129}Xe polarization that are within 10% of that measured [Wagshul and Chupp, 1994, Walker and Happer, 1997, Smith, 1998, Appelt et al., 1998].
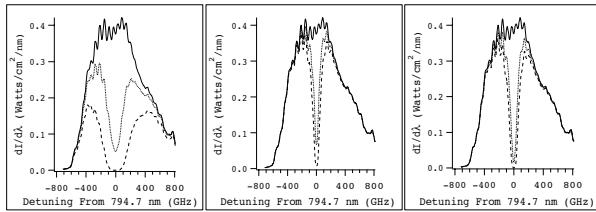

Figure 3: Profile of intensity vs. wavelength for a typical GaAl^{x}As^{1-x} LDA (from Optopower Corp.), indicated by a solid line. The total power output per laser is about 15 watts. The dotted and dashed lines show the laser profile 5 cm and 10 cm into the cell, respectively, for cell parameters of: 10 amagat of ^{3}He and 0.1 amagat N$_2$ at 180°C (left); 0.1 amagat of ^{129}Xe, 0.2 amagat N$_2$, and 2.7 amagat He at 110°C (center); and 2.2 amagat of ^{129}Xe, 0.2 amagat N$_2$, and 0.5 amagat He at 110°C (right).

The requirement for significant Rb polarization is $\gamma_{opt} \gg \Gamma_{SD}$. For ^{3}He, a large portion of the initial laser spectral profile is useful. In figure 3 a, we show the spectral profile at three positions along the axis of the cell for ^{3}He density of 10 amagat with 0.1 amagat N$_2$. As light burns its way into the cell, the central portion of the spectral profile is absorbed more strongly than the wings. Therefore, the front of the cell is essentially polarized by the near–resonance light. The more off–resonance light polarizes a greater portion of the cell's length and is more important in the back of the cell. The large optical thickness of Rb typically used for ^{3}He polarization ([Rb] = 10^{14-15}/cm^3) is the main reason polarization with LDAs can be so effective. The pressure broadening of the Rb absorption line is of secondary importance in most cases; in fact, the gains due to pressure broadening tend to saturate above 4-5 amagat of ^{3}He.

The situation is quite different for ^{129}Xe. The spin destruction rate of Rb due to ^{129}Xe is so much greater than that due to ^{3}He that much greater laser intensity or spectral density (or both) is required to satisfy $\gamma_{opt} \gg \Gamma_{SD}$. Consequently, only a much narrower part of the LDA spectrum is useful for ^{129}Xe, even at very low xenon concentration, as illustrated in figures 1b and 1c. Broadening the absorption line with a buffer gas such as helium, which does not appreciably increase Γ_{SD}, can significantly increase the power absorbed from the LDA spectrum, though it is only practical to increase the absorption line to approximately 0.5 nm with 10 amagat of buffer gas [Driehuys et al., 1996].

The problem of balancing trade offs of noble gas polarization, production rates, volumes, and/or magnetization involves exploring a large parameter space. For example, increasing the total density of gas produces pressure broadening of the Rb absorption line, increasing the integral γ_{opt}, but also increasing Γ_{SD}. Greater Rb density increases γ_{SE} but also increases Γ_{SD} and the absorption of the light as it propagates through the pumping cell, reducing γ_{opt} further into the cell. For example, one can produce 60% ^{129}Xe polarization in 7.5 torr-liters per hour per watt of standard LDA laser power. The actual photon efficiency is less than 0.5%, compared to the 4% efficiency for Rb-^{129}Xe prediction [Walker and Happer, 1997]. A standard liter would require about 100 watts. For ^{3}He, over 50% polarization of more than 1 liter with 30 watts of laser power has been achieved.

Significant improvement of ^{129}Xe polarization is possible if the LDA light is spectrally narrowed. In figure 4 we show a calculation of the expected Rb and ^{129}Xe polarizations for different combinations of xenon density, temperature i.e. Rb density, etc. for 15 watts of laser power. The total pressure is held constant at 2000 torr; for example with 500 torr xenon, we use 100 torr N$_2$, and 1400 torr helium. We show results for two cases: low xenon density, i.e. 100 torr xenon and high helium buffer gas density suggested by Dreihys et al. (1996); and high xenon density 1500 torr xenon used by Rosen et al. (1999). Narrowing LDA spectra provide significant gains in either case. The width parameter for the LDA is essentially a measure of FWHM of the spectrum. We emphasize that narrowing in this case does NOT mean that the lasers need to be single mode as in the case of cooling/trapping/BEC.

Recent progress on narrowing off the shelf LDAs in external cavities [MacAdam et al., 1992] has been reported [Nelson et al., 1999] and [Zerger et al., 1999]. For example, the Littman-Metcalf configuration has been used with 2 watt off–the–shelf LDAs. The spectral profiles for 1.0-1.5 watts output have FWHM 20–30 GHz, and the central frequency could be tuned over several nm. Simulations of the expected performance show that a single 15 watt LDA could be replaced by a 3 watt external–cavity
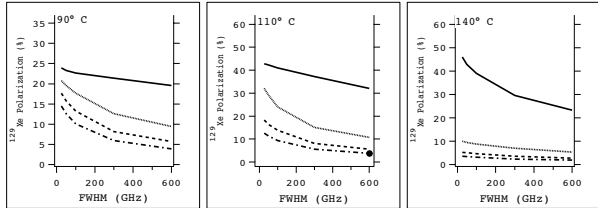
Figure 4: Calculated ^{129}Xe polarization as a function of the LDA line width (FWHM). For each temperature, curves for 0.13 amagat, 0.65 amagat, 1.3 amagat, and 2 amagat of ^{129}Xe are shown from top to bottom, respectively. A constant total density of 2.8 amagat is maintained by loading with helium buffer gas. The solid dot on the 110° shows the measured ^{129}Xe polarization reported by [Rosen et al., 1999].

LDA. With the recent commercial availability of 4 watt broad area LDAs, 3 watts may be possible with a single device. The 2 watt LDA is similar to a single facet of a typical multi–array bar. For most commercially available CW bars, the filling factor is only 30%, and efficient optical feedback from the grating would be difficult. However, bars that are intended for pulsed use are available with filling factors up to 90%. Thermal management problems limit the duty factor of these in normal operation, but reliable operation might be feasible for 10 watts or more.

2.2   Metastability Exchange

In the metastability exchange scheme, a sample of polarized ^{3}He atoms is excited by a weak electric discharge so that a fraction of the atoms ($\sim 10^{-6}$) is in the metastable 2^3S_1 state. This long-lived state can be optically pumped to the 2^3P_0 and $2^3P_{1,2}$ states by 1.083 μm circularly polarized light. For example, the 2^3S_1 state is split into hyperfine levels with $F = 1/2$ and 3/2. Pumping into the $F = 3/2, m_F = +3/2$ state (the C9 line) state produces high atomic and nuclear polarization of the metastable fraction. Resonant exchange of the excitation energy in metastability exchange collisions does not affect the nuclear spin, because the collision duration is short compared to the hyperfine mixing time. Thus, the ground state population attains high nuclear polarization [Colgrove et al., 1963].

In general, the same principles of optical pumping apply to metastability exchange and spin exchange. There are, however, some crucial distinctions. One distinction is the ratio of widths of the atomic absorption line and the Doppler profile. For spin exchange, the high density of ^{3}He or ^{129}Xe and N$_2$ lead to homogeneous collisional broadening of the Rb absorption line of $\approx$ 18 GHz/amagat for ^{3}He

and 14 GHz /amagat for N$_2$ [Che'en and Takeo, 1957]. This greatly exceeds the natural (5.7 MHz) and Doppler widths. Under these conditions, broad–band laser light, from standing wave lasers or laser diode arrays, is effective for optical pumping [Wagshul and Chupp, 1989, Cummings et al., 1995]. For metastability exchange polarization of ^{3}He, the densities are hundreds of times less and Doppler broadening is dominant. Effective optical absorption by all of the atoms requires careful matching of the laser frequency distribution to the Doppler distribution. Another distinction between spin exchange pumping and metastable pumping is optical thickness. We can define an absorption length for polarized resonant photons with $m_l = +1$

$$\lambda_0 = 2([m]\sigma_0\rho(-1/2))^{-1} \qquad (17)$$

where $[m]$ is the number density of metastable atoms or the alkali–metal vapor, and σ_0 is the resonant absorption cross section for unpolarized light. For spin exchange pumping the absorption length is less than the dimension of the optical pumping vessel leading to the radiation trapping problems discussed earlier. λ_0 is generally more than 1 meter for metastability pumping, and radiation trapping does not present any limitations. Under optimum conditions, samples of ^{3}He gas at a density $1.5 \times 10^{16}/$ cm^3 can be pumped to an equilibrium polarization of over 80% with polarization rates of 10^{18} atoms/sec. The dependence of the equilibrium polarization and polarization rate on gas pressure, discharge level and frequency has been studied in detail by [Lorenzon et al., 1993].

Metastability exchange polarization of ^{129}Xe in a discharge has been studied by a few groups with little success [Schaerer, 1969, Lefevre-Seguin and Leduc, 1977]. Though electron polarization in the metastable states indicates effective optical pumping, the discharge may induce excessive nuclear spin relaxation. As an alternative, the metastable $5p^56s$ J=2 state may be populated by two photon laser excitation with (λ=317 nm), or a metastable atomic beam used to separate the discharge from the optical pumping region. These methods will probably not become practical for producing large quantities of polarized ^{129}Xe, but may be useful to study the physical processes at work.

2.2.1   Lasers for Metastability Exchange

The success of metastability exchange based ^{3}He applications has also been strongly supported by laser developments. The first lasers for 1083 nm were color center F$^+$+NaF. Two Nd based laser materials, Nd:Yap [Schaerer and Leduc, 1986, Bohler et al., 1988] and Nd:LNA [Hamel et al., 1987] are now available. Five watts of laser power at the helium transition is routinely obtained by pumping a crystal of Nd:LNA with a CW, krypton arc-lamp in a commercial Nd:YAG cavity. The laser can be tuned to the different pumping lines by use of a solid uncoated etalon in the cavity. [Aminoff et al., 1989]. LDA pumped LNA lasers have also been used [Hamel et al., 1987]. The most recent laser development for metastability pumping of ^{3}He is the diode pumped fiber laser and fiber laser amplifier [Goldberg et al., 1998, Lee et al., 1999].

2.3 Polarization and Delivery Systems

Several devices combine optical pumping and polarization with delivery of the polarized gas to a subject or a storage container. For ^{3}He, the basic designs used for polarized targets are applied for both metastability exchange and spin exchange pumped systems. The metastability exchange systems have a valved port that connects to a transport container. Gentile has recently presented a relatively compact and inexpensive compressor that may see wide use [Gentile et al., 1999]. For spin exchange systems an additional valve of the appropriate material is straight forward. With ^{3}He polarization relaxation times of several days typical in glass containers, transport almost anywhere can be contemplated.

For ^{129}Xe, the high rate of Rb electron spin depolarization in spin–rotation collisions limits the rate of ^{129}Xe production, and a method of accumulation is essential. Cates, Happer, and co–workers have shown that frozen and liquid xenon provide very long nuclear spin relaxation times for ^{129}Xe [Cates et al., 1990, Sauer et al., 1999], and that freezing is an ideal accumulation method [Driehuys et al., 1996]. Relaxation times are on the order of an hour at liquid N_2 temperatures and days at liquid He temperatures [Gatzke et al., 1993].

For human studies, it is sufficient to collect the polarized gas in a plastic bag, where it is held for several minutes before inhalation and a breath–hold. For animal studies, voluntary breathing is not possible, and delivery to the animal requires a polarized gas ventilator. There are many technical difficulties, and very few such ventilators have been constructed [Hedlund et al., 1999, Rosen et al., 1999].

Delivery of polarized gas by shipping from a geographically centralized production facility is one possible operating procedure for the future of medical imaging. In the case of ^{3}He, relaxation times of several days are routine in clean, uncoated, glass containers [Middleton et al., 1993, Chupp et al., 1996], and all that is needed is a portable holding field magnet. Magnetic fields of 10-20 Gauss are sufficient to dominate the magnetic field gradients expected in normal commercial shipping. Both battery operated wire wound coils [Hasson et al., 1999a] and permanent magnet systems [Surkau et al., 1999] have been developed. If liquid He transport of polarized ^{129}Xe becomes practical, its shipment would also be feasible.

3 Basics of MRI

Conventional magnetic resonance imaging (MRI) creates a map of the distribution of water protons in the body and has become one of the most versatile and powerful imaging methods in clinical medicine [Wehrli, 1995]. MRI uses static, RF, and gradient magnetic fields to create images. A large, static magnetic field, B_0, generally between 0.5 to 1.5 Tesla creates an axis of quantization, energy level separation, and energy level population difference for the spin states. A radio frequency field, $B_1(t)$, oscillating at the proton Larmor frequency causes transitions between the spin states and converts longitudinal magnetization into detectable transverse magnetization. Finally, pulsed magnetic field gradients, $\frac{\partial B_z}{\partial x}(t)$, $\frac{\partial B_z}{\partial y}(t)$, or $\frac{\partial B_z}{\partial z}(t)$, are used to both localize and spatially encode the nuclear spin magnetization in order to create an image. Here we present a synopsis of conventional MRI. A complete treatment can be found elsewhere [Callaghan, 1991]. In addition, we review specific aspects of MRI related to imaging laser-polarized noble gases.

3.1 Nuclear Magnetic Resonance

MRI is an application of NMR [Abragam, 1961] with the fundamental relationship given by the Larmor equation,

$$\omega_0 = \gamma B_0. \tag{18}$$

The precessing spins are detected by tipping the magnetization by an angle α with a radio frequency pulse, $B_1(t)$ applied orthogonal to the B_0 field. The signal recorded as a function of time in a pick–up coil is,

$$s(t) \propto \omega_0 M \sin \alpha \ e^{-i\omega_0 t}, \tag{19}$$

where M is the total magnetization of the system, and α is the "tip angle" of the magentization relative to the axis defined by B_0.

3.2 One-dimensional imaging

Lauterbur realized that a map of the spatial distribution of the magnetization could be obtained by acquiring the NMR signal in the presence of a magnetic field gradient [Lauterbur, 1973]. The frequency of the nuclear spin is then directly proportional to the position of the spin and given by,

$$\omega(x) = \gamma(B_0 + xG_x) \tag{20}$$

where x is the position of the spin and G_x is the gradientof B_0 along the x axis:

$$G_x = \frac{\partial B_z}{\partial x}. \tag{21}$$

The time evolution of the transverse magnetization is given by,

$$
\begin{aligned}
s(t) &= \kappa M(x) \ e^{-i\gamma(B_0 + G_x x)t} \tag{22}\\
&= \kappa M(x) \ e^{-i\gamma B_0 t} e^{-i\gamma G_x x t} \tag{23}
\end{aligned}
$$

Where κ is a calibration constant that depends on ω_0, α, and electronic and geometric factors. The only interesting component of $s(t)$, from an imaging point of view, is the additional frequency due to

the magnetic field gradient. Moving into a reference frame rotating at ω_0, the time evolution of the magnetization is given by,

$$s_\rho(t) = \kappa M(x) \, e^{-i\gamma G_x x t}. \tag{24}$$

The signal $s_\rho(t)$ is detected by mixing signals from an oscillator at ω_0 (≈ 64 MHz at 1.5 T) with $s(t)$. One practical consequence of detection in the rotating frame is that the signals can be sampled at audio frequencies rather than RF frequencies. Again, see [Callaghan, 1991] for a complete description.

We now consider a one dimensional distribution of spins along the x-axis. The time evolution of the magnetization is given by

$$s_\rho(t) = \kappa \int_x M(x) \, e^{-i\gamma G_x x t} dx \tag{25}$$

$$= \kappa \int_x M(\omega) \, e^{-i\omega(x)t} dx \tag{26}$$

This is the fourier transform of $M(x)$. Mansfield and Grannell showed that a one-dimensional image could therefore be created by taking the a fourier transform of the NMR signal in the presence of a magnetic field gradient [Mansfield and Grannell, 1973].

$$M(\omega) = \frac{1}{\kappa} \mathcal{F}(s_\rho(t)) \tag{27}$$

3.3 MRI and k-space

For imaging, the goal is to create a plot of the intensity of the magnetization as a function of a spatial coordinate. A more appropriate representation for MRI is a coordinate system with spatial dimensions x and inverse spatial dimensions k_x where,

$$2\pi k_x = \gamma G_x t. \tag{28}$$

Equation 26 can then be rewritten

$$s(k_x) = \int_x M(x) \, e^{-i \, 2\pi k_x x} dx \tag{29}$$

In this formulation, k_x and x are the conjugate fourier variables. The fourier transform with respect to k_x provides a one dimensional map of the magnetization. The applied gradient, and hence k_x, may be time dependent:

$$2\pi k_x(t) = \gamma \int_{\tau=0}^{t} G_x(\tau) d\tau \tag{30}$$

$$s(k_x) = \int_x M(x) \, e^{-i \, 2\pi k_x(t)x} dx \tag{31}$$

Generalizing to two dimensions, we then have,

$$s(k_x, k_y) = \int_x \int_y M(x,y) \, e^{-i \, 2\pi [k_x(t)x + k_y(t)y]} dx dy \tag{32}$$

Much of the progress in MRI over the last decade has been made by controlling the amplitudes and durations of gradients to appropriately sample k–space. These advances have been made possible by improvements in the hardware that produce the magnetic field gradients.

It is important to realize that each point acquired in k-space is spread throughout real space. The point at $k_x = 0$ represents the DC component of the magnetization and is proportional to the magnitude. As $|k_x|$ increases, we measure the fourier coefficients of higher frequency terms. By summing together all of the fourier components in real space, one obtains an image of the magnetization. Artifacts in MRI arise because some of the terms in k-space are not sampled correctly or are lost. For example, a beating heart introduces time dependence not due to $G_x(t)$. The artifact does not appear at one location in real space, rather it is spread according to the sampling error in k-space. A solution to such an artifact is cardiac gating of the signal, triggered by heart monitors.

Another important concept in k-space is prephasing and rephasing of transverse magnetization. Applying a gradient adds a phase to the spins that depends on their position in the sample.

$$\phi(x) = \gamma \int k_x(t)x dt \tag{33}$$

If the direction of the gradient is reversed, the spins at each position acquire an opposite phase. When the $\int G_x(t)dt$ of the two gradients is of equal magnitude, all transverse magnetization is in phase and a gradient echo occurs. In the language of k-space, we first move to a point where k_x is negative. Changing the sign of the gradient changes the direction we move in k-space. The gradient echo occurs when we traverse the point where $k_x = 0$. Most pulse sequences are designed to symmetrically sample k-space in order to maximize signal-to-noise.

3.4 Imaging Sequences

In most cases an MRI tomograph is a two dimensional image of a slice of the body. The slice is isolated by selective excitation of spins along the third dimension. The spatial information is encoded by either frequency dispersion or phase dispersion as discussed in the sections below.

3.4.1 Selective Excitation

Slice selection is typically accomplished by simultaneous application of a magnetic field gradient and a shaped RF pulse with relatively long duration (1 - 10 ms) and correspondingly narrow bandwidth.

This creates a frequency ramp along the direction of the gradient, and the shaped RF pulse excites spins only within a relatively narrow slice. The sinc pulse, $\frac{\sin(t)}{t}$, is the most common because its fourier transform is a rectangle. In practice, the sinc shape does provide a reasonable approximation of a rectangular pulse in space coordinates. The combination of a gradient and a frequency selective pulse only excites spins within a region defined by,

$$\Delta z \approx \frac{2\pi}{\gamma G_z \tau} \tag{34}$$

where G_z is the strength of the magnetic field gradient and τ is the duration between the first zero crossings of the sinc pulse.

3.4.2 Back Projection Imaging

Back projection imaging in MRI detects the NMR signal in the presence of a magnetic field gradient, applied immediately after the slice selective RF pulse. This was the first type of imaging to be performed [Lauterbur, 1973] and is most directly related to other imaging methods such as CT or PET. For the most part, back projection imaging has been replaced by fourier imaging. However, it still maintains a niche in studies of tissues with a short transverse relaxation time, T_2. In laser polarized noble gas imaging, back projection imaging is useful because all views acquired contain the DC component of k–space, which is proportional to the total intensity of the image. Therefore, if image intensity changes from pulse to pulse due to a different amount of gas, it is possible to normalize the acquired signals for proper reconstruction. This is not possible in fourier imaging sequences such as gradient echo imaging.

The pulse sequence needed for two dimensional back projection imaging is shown if figure 5. The frequency selective RF excitation pulse only excites spins in a slice of magnetization along the z-axis in the magnet. Signal acquisition commences immediately after the RF pulse is applied, and the NMR signal is recorded in a constant magnetic field gradient. The direction of the applied gradient is varied by changing the magnitude of the x gradient and the y gradient according to .

$$G_x = G\cos(\phi_i) \tag{35}$$
$$G_y = G\sin(\phi_i) \tag{36}$$

The different amplitudes in the x projection and y projection gradients are represented in figure 5 by the lines of different heights. Each radial step in k–space corresponds to a different value of ϕ_i. For each step, a slice selective pulse is followed by application of the gradients during which the the MRI signal is acquired. Typically ϕ is varied from 0 to 2π in 128 steps. The sampling of k–space, shown in figure 6, is radial. Back projection images are reconstructed with a specialized algorithm and not by a two dimensional fourier transform.
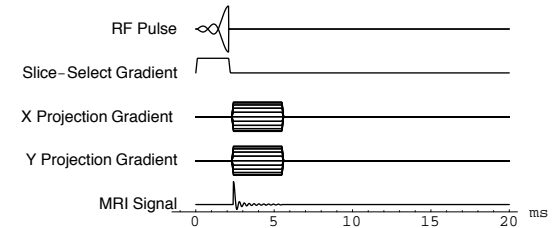

Figure 5: Pulse sequence for Back Projection imaging in two-dimensions. The slice–selective gradient and the frequency–selective RF pulse only excite spins in a slice or slab along the z-axis. The half sinc slice–selective pulse does not require that the transverse magnetization be refocused. The two projection gradients are varied in a sinusoidal pattern.
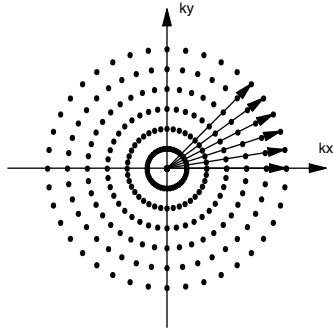
3.4.3 Gradient Echo Imaging

All the elements of two-dimensional fourier MRI are contained in the gradient echo imaging sequence shown in figure 7. Slice selection and read-out gradients are applied as in back projection. The main difference is phase-encoding, first proposed in [Kumar et al., 1975] and later modified in [Edelstein et al., 1980]. Phase encoding now forms the basis of many MRI pulse sequences. In phase encoding, phase dispersion occurs during an interval $t1$ before the signal is acquired during the interval $t2$. The duration of $t1$ or the phase–encode gradient can be varied to step through k_y–space, with $t1$ fixed. Discrete samples are acquired during the interval $t2$ to form a two dimensional dataset. The two-dimensional fourier transformation yields a correlation spectrum in $f1$–$f2$ space or real space.
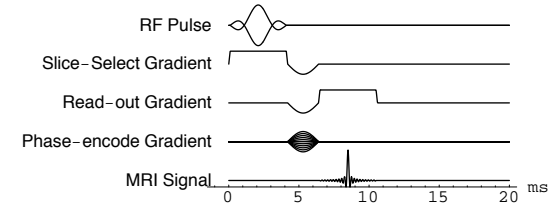

Figure 6: Sampling of k-space by back-projection imaging. In this example, we illustrate just the first few sampled rays obtained by adjusting the gradients according to equation 36

Figure 7: Gradient echo imaging (GRAS or FLASH). Magnetization is sampled in k_x and k_y as shown in figure 8. A two-dimensional fourier transform of uniformly sampled k-space creates the image.

The slice selective pulse in the back-projection imaging sequence of figure 5 is a self-refocussing pulse, allowing the magnetization to be sampled immediately following the RF pulse [Geen and Freeman, 1991]. In general one needs to apply a slice refocussing gradient of opposite magnitude after the RF pulse so that the spins are in phase at the beginning of acquisition. This is shown in figure 7. The area of the negative gradient must be one half the area of the slice selection gradient pulse. At the same time, the read-out dimension is prephased and the phase encoding gradient is applied. Prephasing in the read–out dimension k_x is done to allow symmetric sampling of k-space by first moving in the negative k_x direction before the read–out gradient moves in the positive k_x direction. Phase encoding gradients are applied along the y–dimension. Part of the trajectory through k-space during the gradient-echo
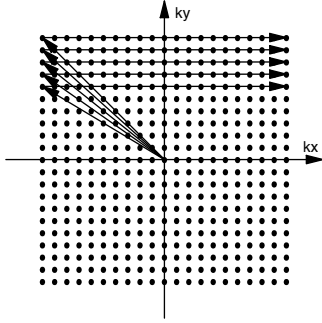
Figure 8: Sampling of k-space by the gradient echo pulse sequence. The phase-encode gradient varies from scan to scan and allows complete sampling of k_y. The readout gradient is prephased to $-k_x^{max}$ and runs to $+k_x^{max}$. The resolution of the image is determined by the value of k_x^{max} and the field-of-view of the image is determined by the step size in k-space.

sequence is shown in figure 8. Starting in the middle of k–space particular values of k_y and k_x are determined by the phase-encode and read-out prephase gradients. The amplitude of the phase-encode gradient is changed for the next step to move to a different point in k_y. By continuing to raster across k_x for the different values of k_y, a complete and even sampling of k-space is achieved. In typical imaging sequences, k_x is acquired with 256 datapoints and k_y with either 128 or 256 datapoints. Each value of k_y requires repeating the sequence. This is not true for k_x, which is called the free dimension in MRI. The number of k_x points is typically determined by the desired resolution and the transverse relaxation time, T_2.

3.4.4 Chemical Shift Imaging

Chemical shift imaging or CSI is a hybrid application of imaging and spectroscopy. CSI is used to obtain spatially resolved spectral information or images of specific spectral components. Since gradients, which would disperse frequency across spatial dimensions, cannot be applied during acquisition, phase encode gradients are applied along either one, two, or three dimensions. A two-dimensional chemical shift imaging pulse sequence is shown in figure 9. After the gradients are applied, the magnetization

freely precess in the B_0 field so that a frequency spectrum can be measured. This pulse sequence has been used to separate the different components of xenon magnetization in the rat brain and in the rat body [Swanson et al., 1997, Swanson et al., 1999b] as described section 5. CSI requires discrete steps through each dimension of k–space, and is much slower than back projection and gradient echo sequences, which step through only one dimension in k–space. To collect a 16 by 16 image, 256 different acquisitions are required.
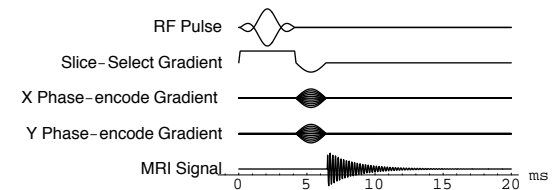

Figure 9: Two dimensional chemical shift imaging (CSI) sequence. After slice selection, phase encode gradients are simultaneously applied along k_x and k_y. After the gradients are applied, the magnetization precesses freely in the B_0 field so that a frequency spectrum can be measured.

3.5 Contrast in MRI

In tissue, the proton density varies only slightly, and MRI contrast therefore depends on changes in the magnetization characterized by relaxation times. The longitudinal or spin-lattice relaxation time T_1 determines the time required for the spin polarization to return to equilibrium following excitation by a radio-frequency pulse. If the spin magnetization is flipped by $\pi/2$, the longitudinal magnetization recovers according to,

$$M_z(t) = M_z^0(1 - e^{-t/T_1}). \tag{37}$$

Figure 10: Conventional proton MRI tomographic images of the human brain. The images were acquired using spin–echo sequences. The detected magnetization depends on T_1 or T_2^*, depending on the echo time. This provides the contrast. The white matter and grey matter in each lobe of the cerebrum is distinguished in the T_1 weighted image on the left. Cerebral spinal fluid and tissue are distinguished in the T_2 weighted image on the right.

The transverse or spin-spin relaxation time T_2 is the time constant for decay of the transverse (x and y) components of magnetization.

Both T_1 and T_2 weightings require the spin–echo sequence. The spin–echo sequence is similar to the gradient echo sequence, however a π pulse refocuses spins that dephase in the intrinsic magnetic field inhomogeneities of the sample. The π pulse is typically applied ≈ 10 ms and ≈ 50 ms after the initial RF pulse for T_1 and T_2 weighting respectively. In brain imaging for example, proton concentrations in white matter and grey matter are nearly equal, in contrast to the relaxation times given in table 1. For cerebral spinal fluid (CFS) motion effectively increases T_2. The relaxation time differences are exploited to produce images such as those shown in figure 10.

Table 1: Typical relaxation times for protons in brain tissue [Bottomley et al., 1984].

	T_1	T_2
Grey Matter	1000 ms	110 ms
White Matter	650 ms	70 ms

3.6   Low Field Imaging

NMR with nuclei polarized by laser optical pumping is less dependent on large magnetic fields than conventional NMR, and the potential of low–field imaging has emerged. The signal to noise ratio (SNR) is the important parameter, and we therefore consider both signal and noise. For conventional, NMR, the signal S due to a nuclear spin $I = \hbar/2$ (for ^{1}H, ^{3}H, and ^{129}Xe) with concentration $[I]$ is proportional to the product of precession frequency (ω) and magnetization:

$$S \propto \omega \mu_I [I] P \qquad (38)$$

where $I\omega = \mu_I B$ and the brute–force polarization is $P_I \approx \frac{\mu_I B}{kT}$. Thus

$$S_{brute} \propto \mu_I^3 B^2 [I]. \qquad (39)$$

In contrast, for NMR with laser polarized nuclei, P_I is independent of field, and

$$S_{laser} \propto \mu_I^2 B [I] \qquad (40)$$

The most important MRI noise sources are Johnson noise due to the pick–up coil resistance, R_c, amplifier noise, and dissipation in the sample due to loading characterized by R_s. Skin depth effects generally increase the coil resistance so that $R_c \propto \sqrt{B}$. The signal to noise ratios for brute–force and laser polarization for fixed bandwidth are

$$SNR_{brute} \propto \frac{B}{\sqrt{1 + \alpha B^{-3/2}}} \qquad SNR_{laser} \propto \frac{1}{\sqrt{1 + \alpha B^{-3/2}}} \qquad (41)$$

where $\alpha \approx (0.2 \text{ T})^{-3/2}$ [Edelstein et al., 1986]. This shows that above about 0.2 T, the signal to noise ratio for laser polarized NMR and MRI increases very little, i.e. is approximately independent of B.

There are many advantages that may be gained from NMR and MRI at lower fields. The cost of magnets is less, open geometry permanent and conventional magnets may provide more friendly NMR scanners (important for pediatrics), high field effects such as susceptibility dependence may be less. Low field work has been most effectively pursued by [Darrasse et al., 1998]. They have shown that the combination of 0.1 T magnet and a low–polarization metastability pumped ^{3}He polarizer can produce lung images with resolution comparable to standard ^{133}Xe nuclear medicine techniques as shown in figure 11. One-dimensional images of polarized ^{3}He have been to study diffusion effects [Saam et al., 1996]. Very low field imaging, at 0.003 T has been demonstrated by Walsworth and collaborators [Tseng et al., 1998].

4   Imaging Polarized ^{129}Xe and ^{3}He Gas

Though either ^{3}He and ^{129}Xe may be used for gas imaging, the majority of lung ventilation imaging studies, have used ^{3}He. Helium has a number of advantages over xenon for creation of high-resolution
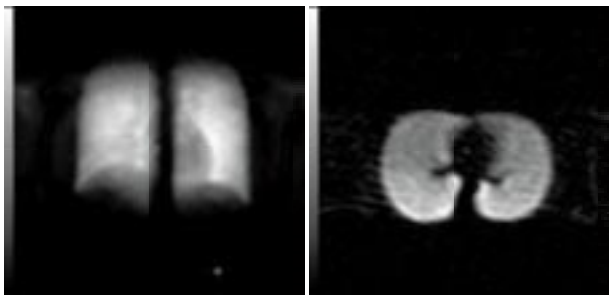
Figure 11: Lung images of a healthy volunteer produced with laser polarized ^{3}He at 0.1 T using multi spin-echo sequence. The slice thickness is 5 cm. Less than 30 cm^3 of ^{3}He with initial polarization 15% was mixed with a buffer gas just prior to inhalation. *Image Courtesy of Laboratrioe Kastler–Brossel of ENS, Paris. Used with permission.*

gas images: the magnetic moment of ^{3}He is nearly three times larger than that of xenon, and it has generally been easier to create high magnetization with ^{3}He. ^{3}He polarizations are generally of 20%– 50% whereas typical ^{129}Xe polarizations are currently 5%. A recent study imaging both gases concluded that in general helium is approximately 10 times more sensitive than xenon for MRI studies [Moller et al., 1999a].

Helium also has fewer biological effects than xenon. Helium is biologically inert and the only consequence of helium inhalation (apart from the well known change in voice pitch) is the risk of lowering the blood oxygen content due to oxygen being removed from the inhaled gas. Xenon on the other hand, is anesthetic at concentrations greater than 35%. These effects are well known and have been addressed in CT studies where xenon is used to measure regional cerebral blood flow (rCBF) by monitoring the spatial and temporal attenuation of x-rays

Though helium provides greater signal strength and fewer medical complications, a major concern for widespread clinical studies with helium will be the limited supply of ^{3}He discussed earlier. Most studies are performed with ^{3}He gas with an isotopic concentration of approximately 99% at a cost of approximately 100-150 USD/liter. Xenon is present in the air at a concentration of approximately 0.04%. The abundance of the spin 1/2 isotope, ^{129}Xe, is 26.44%. Naturally abundant xenon can be purchased for approximately 10 USD/liter. ^{129}Xe enriched to approximately 75% can be purchased for about 300 USD/liter. This price is determined primarily by demand and could drop dramatically

if specific clinical uses are identified.

4.1 MRI of polarized gas: general concerns

4.1.1 Sampling of the magnetization

In conventional MRI, longitudinal magnetization is sampled by an RF pulse and then replenished by relaxation to thermal equilibrium with time constant T_1. For laser polarized gases, the longitudinal magnetization in the body must be replenished by a fresh supply of polarized gas. With each sampling of the magnetization, the RF pulse destroys a portion of the longitudinal magnetization. The non-equilibrium polarization created by optical-pumping would be entirely lost if sampled by a $\pi/2$ RF pulse. Since MRI requires many excitations in order to appropriately sample k–space, $\pi/2$ pulses cannot be used. The gradient echo sequence shown in figure 7 with a small tip angle is the most widely used approach. As the gas is sampled, the longitudinal magnetization decays leaving magnetization after n pulses is given by

$$M_z(n,\alpha) = M_z^0 \cos^n(\alpha) \tag{42}$$

where α is the tip angle. Thus the sampled magnetization in the initial pulses is larger than that in the later pulses if the tip angle is constant. For instance, if the tip angle is 10 degrees, the value of the magnetization at the end will be only 20 percent the initial value for 128 pulses typically used to collect an image. This will cause different fourier components of k-space to have intensities modified by an exponential decay. This leads to blurring of the real space image as each pixel is the convolution of the true magnetization with a lorentzian (the fourier transform of the exponential loss of magnetization to pulsing.) Variable tip angle series have been used to economically use laser pumped magnetization in two species experiments that probe fundamental principles [Chupp et al., 1989, Oteiza, 1992]. An MRI sequence with variable pulse angle that produces the proper intensity of the fourier coefficients in k-space has been proposed [Zhao et al., 1996]. In principle, the variable flip angle sequence has better SNR since all of the magnetization is sampled. In practice, it is difficult to program this sequence on clinical MRI systems and most studies use a constant flip angle.

4.1.2 Diffusion and k–space

The basic description of MRI in section 3 neglected effects due to the diffusion of spins during acquisition. For gas imaging, these effects are large and present many problems, as well as a few opportunities. The main problem stems from the fact the positions and therefore the frequencies of the spins change due to diffusion as k–space is sampled during the read out gradient. Since k–space is sampled along one dimension, we consider the mean path length for one-dimensional self-diffusion $d = \sqrt{2Dt}$ where D is the diffusion constant and t is the time. At one atmosphere xenon has a self–diffusion constant

of approximately 0.06 cm^2/s and helium approximately 2.0 cm^2/s. Therefore, during a typical MRI experiment with a sampling time of about 6 ms, the resolution for ^{3}He is limited to about 1.5 mm. This assumes that the spins are free to diffuse. In the lungs' alveoli and other porous media free diffusion is restricted. This allows measurement of pore size that has recently been applied to lung imaging. A full treatment of diffusion and restricted diffusion can be found in [Callaghan, 1991].

A number of studies have investigated this phenomenon. Edge enhancement of the signal intensity near the walls of rectangular glass cells in one-dimensional images of polarized ^{3}He has been observed [Saam et al., 1996]. These studies were extended to demonstrate image distortion by molecular diffusion during the read out gradient [Song et al., 1998]. In this study, the investigators varied the strength of the gradient to follow the images from the strong diffusion regime to the weak diffusion regime. In another study using thermally polarized xenon gas diffusion was used to measure the tortuosity and the surface-to-volume ratio in a system of glass beads[Mair et al., 1999]. Work from the same group also showed that the gas diffusion constant can be measured in a single experiment [Peled et al., 1999].

4.2   Airspace Imaging

Lung ventilation imaging is currently based on nuclear medicine scintigraphy of either ^{133}Xe or aerosol sprays with Tc. Laser–polarized noble–gas imaging research with animals and human subjects has already shown that tomographic (slice selected) high resolution images can be produced. A comparison of ^{133}Xe scintigraphy and laser–polarized ^{3}He images is shown in figure 12. The first human ventilation studies with ^{3}He were performed in Mainz[Ebert et al., 1996] and at Duke. The group at Mainz (see figure 13) has continued with more clinical studies of volunteers with diagnosed lung diseases [Bachert et al., 1996, Ebert et al., 1996, Kauczor et al., 1997]. Other studies have looked at helium images of from the lungs of smokers [de Lange et al., 1999] and find ventilation defects in the few cases studies. In fact even apparently healthy, active, volunteers have ventilation defects that are revealed in the high resolution laser polarized ^{3}He MRIs [Mugler et al., 1997]. A study of subjects with chronic asthma suggests that ventilation defects may allow a measure of the progression and treatment of the disease[Altes et al., 1999]. Though it will be some time before the utility of high resolution lung images is clarified, it is clear that they provide new information and raise new questions.: for example, what are the mechanisms of signal destruction in diseased lungs [Kauczor et al., 1998]. The lungs are not the only organ amenable to gas imaging. The sinus cavities [Rizi et al., 1998] and bowel [Hagspiel et al., 1999] can also be imaged by using laser-polarized ^{3}He or ^{129}Xe.

Animal studies provide appropriate disease models for eventual clinical studies. An advantage of using a small animal model is that the amount of polarized gas needed to create an image is significantly reduced compared to an equivalent human study. Impressive results using specialized small pick–up coils to attain high resolution images of ^{3}He in animal models have been obtained by the group by the group at Duke University. They showed the first *in vivo* images of helium in the
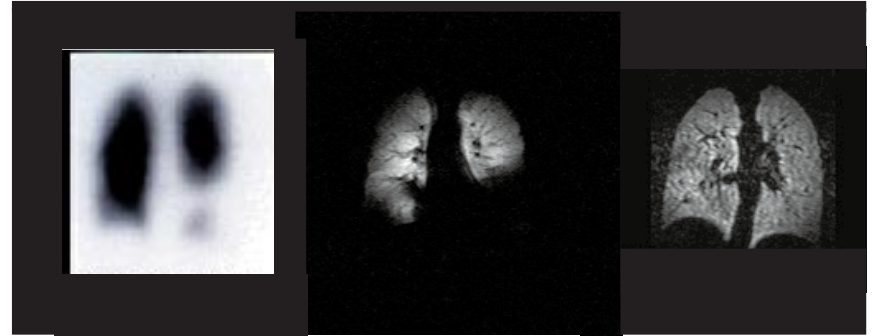

Figure 12: Three lung images: Left: A ^{133}Xe nuclear medicine scan of a patient with chronic obstructive pulmonary disease (COPD). Center: A laser polarized ^{3}He MRI of the same patient. Right: Laser polarized ^{3}He MRI of a healthy volunteer. *Image Courtesy of the University of Virginia. Used with permission.*

lungs using two- and three-dimensional gradient echo imaging [Middleton et al., 1995]. They also have demonstrated that the back projection imaging sequence can be used to reduce problems associated with changes in signal amplitude as k-space is sampled. Figure 14 shows images from a Guinea pig model. These studies also show that one can vary the tip angle to capture either the early or later phases of inhalation. More recent work has concentrated on the magnetic behavior of both ^{3}He and ^{129}Xe gas in the lungs. One study finds that the effective transverse relaxation time (T_2^*) for ^{3}He is approximately 14 ms in the trachea but 8 ms in the intrapulmonary airspaces. For ^{129}Xe, T_2^* is 40 ms in the trachea and 18 ms in the intrapulmonary airspaces. This indicates that the ^{129}Xe interacts more strongly with the tissue of the itrapulmonary airspaces as it crosses the blood gas barrier. The regional variation of the diffusion constant was measured *in vivo* in guinea pigs [Chen et al., 1998].

A study from a group in Lyon examined combining MRI of ^{3}He gas with proton based methods to measure lung perfusion [Cremillieux et al., 1999]. The goal is to provide a regional assessment of lung function. Methods in nuclear medicine typically provide only low resolution images that are
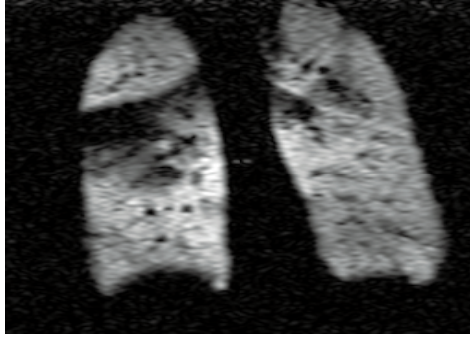
Figure 13: Laser polarized ^{3}He lung image. The patient is suffering from pulmonary artery obstruction due to hydatid disease. The image shows a large ventilation defect in the apical segment of the lower lobe on the right. Surprisingly, this corresponds also to an obstruction of the pulmonary arterial branch. *Image Courtesy of Radiologie Klinik at Mainz University. Used with permission.*

projections through the entire lungs and are not tomographic. Combination of conventional and laser polarized gas MRI has the potential to provide very high resolution images for diagnosis of certain lung diseases such as pulmonary embolism. A collaboration between the Duke and Lyon groups has presented images of the Guinea pig lungs with 2–dimensional resolution of less than 100 microns [Viallon et al., 1999].

4.3   Injection of ^{3}He and ^{129}Xe Carriers

Laser polarized gas dissolved or encapsulated in injectable carriers is also under study [Goodson, 1999]. Since xenon is highly soluble in non-polar liquids, it is possible that images of xenon can be obtained *in vivo* by injection of xenon dissolved in an appropriate carrier. Work in Alex Pines's laboratory at the University of California, Berkeley, has shown that xenon dissolved in different carriers may have a significantly greater SNR than can be created by inhalation of xenon gas [Goodson et al., 1997]. At Duke, laser polarized ^{3}He was trapped in microbubbles and introduced into the tail vein and arterial blood of a rat [Chawla et al., 1998]. This new form of angiography provided high resolution images. Also at Duke, laser polarized ^{129}Xe was dissolved in biologically compatible lipid emulsions (Intralipid
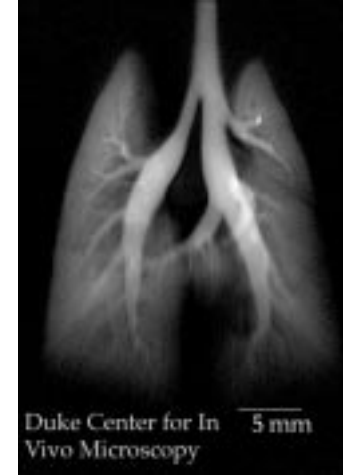

Figure 14: Ventilation images of a guinea pig lung showing the exceptional spatial resolution possible with polarized ^{3}He and the specialized techniques of *in vivo* microscopy. *Image Courtesy of the Center for in vivo Microscopy at Duke University. Used with permission.*

30%) [Moller et al., 1999b]. Measured relaxation times were $T_1 = 25.3 \pm 2.1$ sec, and $T_2^* = 37 \pm 5$ ms. Analysis of magnetization inflow was used to deduce the mean blood flow velocity in several organs. Several other potential carriers have been investigated including perfluorooctyl bromide (PFOB), a blood substitute [Wolber et al., 1998]

5   NMR and MRI of Dissolved ^{129}Xe

In contrast to ^{3}He, which is most useful for imaging air spaces such as the lungs and colon, ^{129}Xe is soluble in blood with $\approx 17\%$ solubility and tissue with varying solubility [Chen et al., 1980]. Many of the biological properties of xenon have been established through research with radioactive isotopes, particularly ^{133}Xe. Xenon freely diffuses across biological membranes including the blood gas barrier

in the lungs and capillary walls between blood and tissue. Xenon is metabolically inert, and is carried to distant organs where it accumulates in tissue. The size of the ^{129}Xe magnetization signal in a specific region of interest can be a measure of the rate of blood flow or perfusion through the tissue. Studies using radioactive ^{133}Xe have shown that xenon can be used in diagnosis and research to measure kidney perfusion [Cosgrove and Mowat, 1974], and cardiac perfusion [Marcus et al., 1987].

Most exciting may be the study of regional brain activation. A variety of techniques has enormously enriched our understanding of the functional organization of the nervous system. The methods of Kety and Schmidt [Kety and Schmidt, 1945] for measuring total blood flow following administration of a metabolically inert gas have been combined with radiotracer imaging techniques to measure changes in regional cerebral blood flow (rCBF) correlated with sensory stimulation, motor activity and inferred information processing in the brain. Early experiments used inhaled or injected gamma-emitting gases such as ^{133}Xe [Lassen, 1980] or ^{85}Kr [Lassen and Ingvar, 1961] to measure altered blood flow in the cerebral cortices. More recently positron emission tomography (PET) methods, most notably those employing ^{15}O-H$_2$O, have been used to measure rCBF [Phelps, 1991]. However PET techniques have intrinsic resolution limited to 2-4 mm due to the range of positrons in tissue and often desire a complementary imaging technique such as MRI or CT for accurate anatomical mapping of the PET functional information. MRI methods are not subject to these intrinsic limitations and can provide functional information and anatomical registration with a single modality and apparatus. Several methods for measuring brain function with MRI have been explored [Shulman et al., 1993], and techniques based on blood oxygen level dependence of proton NMR have demonstrated high spatial resolution [Ogawa et al., 1990], though the physiological basis for the detected changes in signal is not well understood [Shulman et al., 1993].

5.1 Spectroscopy of ^{129}Xe *in vivo*

Figure 15 shows an NMR spectrum of ^{129}Xe from the body and head of a rat that had been breathing a mixture of ^{129}Xe and oxygen gas [Swanson et al., 1999b]. Similar spectra have been observed in humans after a single breath–hold of laser polarized ^{129}Xe [Brookeman, 1998]. The peaks in the rat body spectrum (figure 15 a) have been identified on the basis of work by several authors including the time dependence of the peaks [Wagshul et al., 1996, Sakai et al., 1996, Swanson et al., 1999b], the location of each resonance determined by imaging (see figure 2), and the chemical shifts revealed in *in vitro* experiments [Wolber et al., 1999a]. The chemical shift may also depend on the oxygenation level of the blood [Wolber et al., 1999b] and varies with tissue type.

The spectrum from the head (figure 15 b) reveals at least four peaks in addition to the apparent blood peak at ≈210 ppm. Though there is not yet a definitive identification of the separate tissue types, this does show that several kinds of brain tissue are highly perfused and/or have large partition coefficients for dissolved xenon. An exciting direction for future research is the identification of each chemical shift component and functional study of the differences. It may become possible to identify
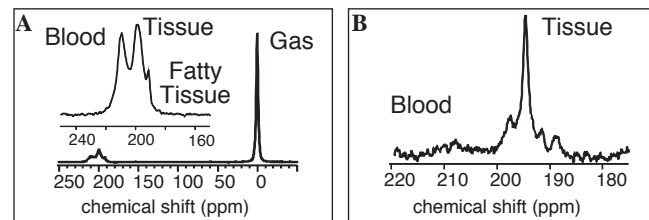

Figure 15: Spectra from the body and head of a rat breathing a ^{129}Xe–O$_2$ mixture. Left: the body spectrum showing signals from gas in the lungs (at 0 ppm), and dissolved in the blood (210 ppm) and tissue (192 ppm and 199 ppm). Right, the spectrum from the head showing several tissue peaks and possibly the blood peak near 210 ppm.

the kinds of tissue involved in specific neurological functions.

5.2 ^{129}Xe Imaging

As ^{129}Xe is carried throughout the body by the flow of blood, it is deposited in tissue with time dependent concentration that depends on several factors including the rate of blood flow, *i.e.* perfusion. Perfusion measurement has many applications ranging from rCBF measurement and research in cognitive neuroscience to assessment of pulmonary, renal, and cardiac health. One key goal of laser polarized ^{129}Xe MRI is development of techniques of perfusion measurement, that is use of ^{129}Xe as a magnetic tracer that uses the chemical shifts to isolate each tissue type. The development of such techniques is discussed in section 5.4.

Images of each chemical shift component of ^{129}Xe can be created using the CSI sequence (described in section 3.4.4) and possibly frequency selective excitation. CSI produces frequency spectra for each pixel as illustrated in figure 16, where we show spectra acquired for each of four adjacent pixels. The pixel map is superimposed on proton images acquired with the spin–echo sequence described in section 3.5. In figure 2, actual images of ^{129}Xe in gas, blood, and tissue are shown. These are magnetization maps of the signal in each of the peaks indicated in figure 15a. An Image of ^{129}Xe dissolved in tissue in the rat head [Swanson et al., 1997] is shown in figure 17.

The images of ^{129}Xe in dissolved phases shown in figure 2 demonstrate some potential medical applications that may emerge in the coming years. Images of the lungs in the gas phase (figures
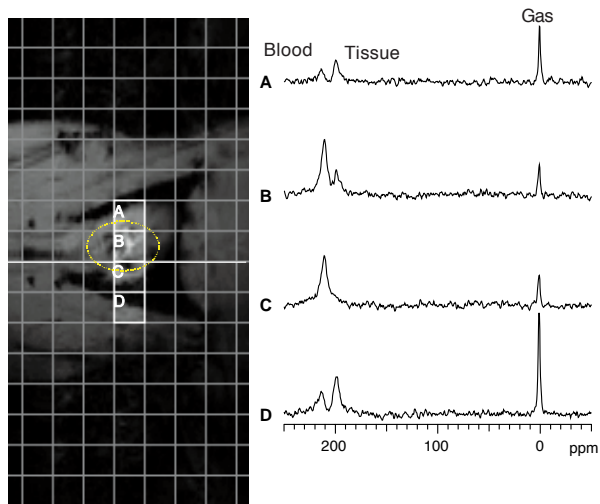
Figure 16: Illustration of the data provided by the CSI imaging sequence. For each pixel, a frequency spectrum is produced. Spectra for four pixels are shown. The background gray–scale image is a proton MRI acquired with the spin–echo sequence. The oval surrounds the heart region.

2A and 2D) show the region of ventilation. In a healthy lung, xenon crosses the blood–gas barrier, appearing also in tissue (figures 2B and 2E) and blood phase images (figures 2C and 2F). We discuss further analysis of lung function in the next section. The blood carries the ^{129}Xe magnetization from the lungs to the left side of the heart. In the heart, the blood phase signal is dominated by pooled blood in the left heart chambers. Perfusion in the healthy heart is indicated by the appearance of ^{129}Xe magnetization in the dissolved tissue and fat phases in the heart also shown in figures 2B and 2E. Restricted blood flow (ischemia) and unperfused regions (infarction) would be revealed by the absence of the dissolved tissue phase in that region.
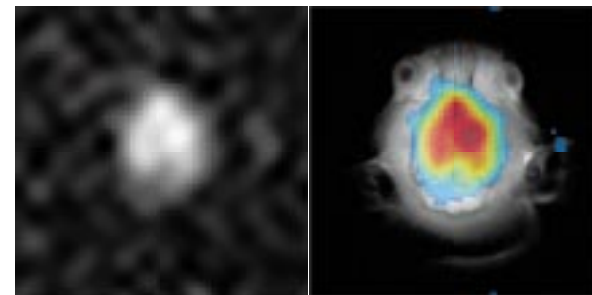

Figure 17: CSI image of ^{129}Xe dissolved in tissue of the rat brain. On the left is the gray scale ^{129}Xe image and on the right is that image false–colored and superimposed on a proton spin–echo image.

5.3 Lung function

The main functions of the lung are ventilation and perfusion. Many problems in the lungs result when there is a ventilation-perfusion mismatch. For example, regions of the lung that are ventilated but not perfused characterize about 70% of pulmonary embolism cases. Tomographic measurement of ventilation and perfusion, combining gas phase imaging in the lungs and ^{129}Xe dissolved phase imaging of the blood and tissue provide a new way to study lung function and may assist in appropriate treatment of lung disease.

The data of figure 2 can be analyzed to extract ratios of blood and gas ^{129}Xe concentrations, shown as images in figure 18. Figure 18a shows that the gas:tissue ratio is relatively uniform except near the trachea and in the peripheral regions of the lung. The gas:blood ratio (Fig. 18b) image shows a similar mismatch in the trachea but also more variation throughout the lungs. Some of this variation may be normal.

Other possible methods of pulmonary MRI using polarized ^{129}Xe are venous injection of dissolved gas (see section4) followed by simultaneous imaging of the blood and gas components and study of the spatial variation in the frequency of the blood resonance, likely related to the oxygen content of the blood. The rich information content of ^{129}Xe spectra and images provides interesting opportunities for pulmonary applications.
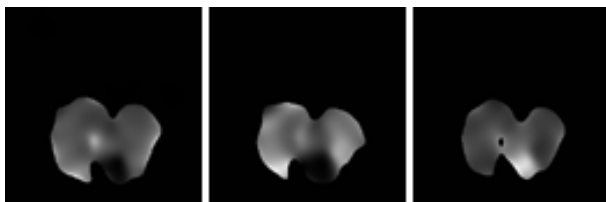
Figure 18: Images of ratios of ^{129}Xe resonances: a.) gas:tissue, b.) gas:blood, c) blood:tissue.

5.4 Time Dependence and Magnetic Tracer Techniques

The time dependence of the different chemical shift components of ^{129}Xe is important in several applications. As we show below, laser polarized ^{129}Xe magnetic tracer can measure blood flow and the dynamics of exchange across blood gas and blood tissue barriers. In general, the time dependence of a chemical shift magnetization component depends on the rate of delivery to the tissue in the region of interest (perfusion) and on the local magnetization relaxation time, T_1. This relaxation time is also, in general time dependent as oxygen concentration changes. Several authors have developed multi–compartment models of ^{129}Xe magnetization time dependence [Peled et al., 1996, Martin et al., 1997, Welsh et al., 1998]. The goal is to measure the time dependence and use the model to extract quantities of interest, in particular T_1 and blood flow independently.

Nuclear medicine methods based on PET are highly developed, however MRI based methods of tissue perfusion measurement may have advantages compared to PET: 1) the chemical shift information allows blood and various tissue types to be isolated; 2) with an entirely MRI based technique, the perfusion map can be anatomically registered with conventional proton images; 3) the resolution is not inherently limited, in the way PET is limited to several millimeters by the range of high energy positrons in tissue; 4) radioactive dose restrictions that limit repeated PET studies do not impact MRI techniques.

In figure 19, we schematically illustrate how MRI of laser polarized ^{129}Xe can be used as a magnetic tracer to measure perfusion. Once inhaled, ^{129}Xe is carried from the lungs to heart, brain, and other distal organs. The signal produced at the frequency of the tissue resonance in a given organ (or pixel in an organ) is a measure of the total ^{129}Xe magnetic moment in the measured volume of tissue. Tissue magnetization, M_T, calibrated in units of the arterial magnetization, M_A, depends on blood flow F and the local magnetization relaxation rate $1/T_1$ in different ways. If M_T is uncalibrated, data can be used to determine relative blood flow.
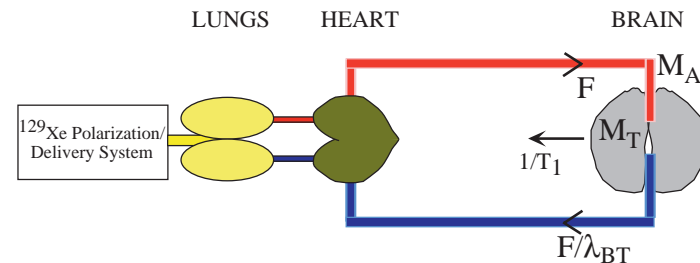

Figure 19: Schematic of the magnetic tracer technique described in the text.

As the blood caries ^{129}Xe with magnetization M_A into tissue, the NMR signal size of the tissue resonance in each volume element of the tomographic image changes with time. The differential equation describing the tissue magnetization (M_T) in a voxel is

$$\frac{dM_T}{dt} = FM_A - (\frac{1}{T_1} + \frac{F}{\lambda_{BT}})M_T \qquad (43)$$

where F is the rate of blood flow in units of $\text{ml}_{Blood}/\text{minute}/\text{ml}_{Tissue}$, and λ_{BT} is the blood-tissue partition coefficient: the ratio of concentrations of xenon in blood to that in tissue. The time constant for relaxation of ^{129}Xe magnetization to thermal equilibrium is T_1. This differential equation is quite similar to that for the standard nuclear medicine formulation describing wash in of a radioactive tracer (*e.g.* ^{15}O-H_2O for PET or ^{133}Xe for SPECT). However there is an extremely important difference: the relaxation time constant, T_1, is not uniform, rather it is generally different in different tissues and blood, and it depends on the blood's oxygenation level [Wilson et al., 1999, Wolber et al., 1999a]. Measurement of dynamics of ^{129}Xe tissue resonance in the rat brain is consistent with $T_1 \approx 30$ s [Welsh et al., 1998]. Techniques have been proposed for separating F and T_1 [Swanson et al., 1999a].

Absolute measurement of F in units of ml/min/ml requires calibration of M_T in units of M_A. This requires measuring the magnetization signal from known volumes of tissue and blood respectively. For quantitative measure of rCBF, it may be possible to image the blood in the carotid artery. For cardiac perfusion, imaging of the pulmonary veins and left heart chambers is possible (see figure 16). One important caveat follows from the small separation of the blood and tissue peaks, about 150 Hz at 1.5T. With the observed T_2^* varying from 2 ms in blood to 20 ms in brain tissue, any NMR pulse that

tips the magnetization of ^{129}Xe in tissue will perturb the blood magnetization. Thus M_A will come to an equilibrium value that is, in general, less than the unperturbed M_A. However, the perturbation can be relatively small with proper design of the pulse shape and phasing and because the rate of blood flow to the region of interest is high compared to the pulse rate $1/\tau$ [Geen and Freeman, 1991]. Another possible complication is that the blood and tissue concentrations may not equilibrate rapidly on the time scale of the imaging experiments (about 1 second) resulting in an apparent variation of λ_{BT}.

5.4.1 Dynamics of Laser Polarized ^{129}Xe *in vivo*

Features of the dynamics of Laser Polarized ^{129}Xe in the lungs, body and brain of rats *in vivo* are shown in figure 20 [Swanson et al., 1999b]. Frequency spectra collected as a function of time were used to study the dynamics of laser polarized ^{129}Xe. Qualitative interpretation suggests that the blood component builds up more quickly and saturates with respect to the lung input function, whereas the tissue component builds up more slowly due to greater tissue capacity for xenon, and falls off more slowly due to the longer intrinsic T_1 in tissue and the relatively slow wash out of xenon. The amplitude of the blood resonance closely follows the amplitude of the scaled gas resonance. The blood resonance plateaus after about 13 s of xenon delivery, but the tissue/plasma peak and the fat peak continue to grow and do not level off, even when xenon delivery is stopped at about 25 s.
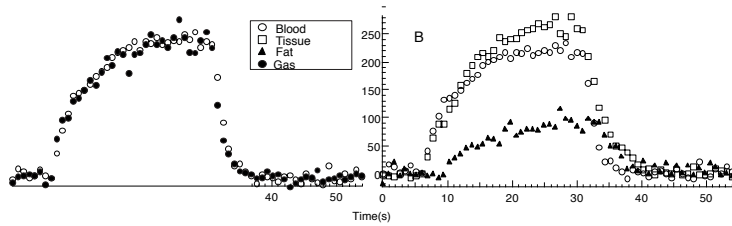

Figure 20: Dynamics of ^{129}Xe gas, blood, and tissue resonances.

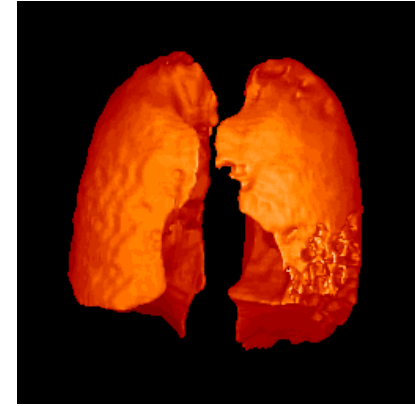## 6 Conclusions – Future Possibilities

Figure 21: A surface rendering of the human lung constructed with laser polarized ^{3}He MRI. *Image Courtesy of the University of Virginia. Used with permission.*

The future is exceptionally bright for research in biomedicine, neuroscience, and materials science with laser polarized rare gas imaging. The scientific problems relating to polarization techniques, delivery of polarized gas with devices and in solutions are challenging, but progress continues. Ventilation images of animals and humans in the US and Europe provide unprecedented resolution and are likely to provide new information, as is often the case when we can look at something with greater sensitivity, precision, and resolution. Figure 21 provides a stunning example. The new techniques possible with ^{129}Xe provide resolution in chemical shift frequency and time that promise to develop into ways of measuring perfusion of specific tissues as well as organs, complementing PET. The potential for a completely quantitative measure of perfusion promises broad application. All of these possibilities have been discussed in this review.

However, research with a new imaging modality does not ensure its application as a medical diagnostic procedure. Among the potential applications of high resolution lung ventilation imaging, colonoscopy, lung function assessment, and perfusion measurement, MRI with laser polarized gases must pass the tests of

1. sensitivity to disease or injury

2. specificity for a unique diagnosis

3. effectiveness based on cost and risk

For example, high resolution lung imaging with ^{3}He has been shown to be clearly sensitive to small ventilation defects – regions of the lung that do not effectively fill with gas in a normal breath. But the question of what specific malady this indicates is currently open. On the other hand, lower resolution ^{3}He or ^{129}Xe lung images, produced with less gas and lower polarization (see figure 11) provide the same ventilation information as a ^{133}Xe nuclear medicine scintigraphy, but without the radiation dose of nearly 1 Rad from a single study. Such lower resolution scans would therefore provide the demonstrated sensitivity and specificity of the widely used nuclear medicine techniques. However the cost of an MRI is currently many times greater a ^{133}Xe nuclear medicine study, and the additional cost of laser polarized gas would significantly increase the cost of an MRI. Low–magnetic–field imaging systems may bring the cost down. Early diagnosis procedures and repeated studies that would be limited by radiation dose may be developed by physicians with these new tools. Pediatric pulmonary medicine may be an important application of the combination of diagnosis without radiation dose and low–field, open–geometry magnets.

With the promise of these and a host of other potential applications, pre–clinical efforts are underway in the US and Europe. In the US, the efforts are organized by the commercial interest that would produce the polarized gas in regional centers and ship it, overnight, to medical facilities. In Europe, a collaboration of industry, academic, and hospital based researchers is developing the pre–clinical program. The goals of both these groups include regulatory approval for administration of polarized gas as a contrast agent and its use for medical diagnosis. Interestingly, the final step in regulatory approval, following demonstration of safety and other issues, is demonstration of efficacy: the sensitivity and specificity for diagnosis of specific maladies that physicians would be likely to use.

7   Acknowledgements

References

[Abe et al., 1997] Abe, K., Akagi, T., Anderson, B. D., Anthony, P. L., Arnold, R. G., Averett, T., Band, H. R., Berisso, C. M., Bogorad, P., Borel, H., et al. (1997). Precision determination of the neutron spin structure function g_1^n. *Phys. Rev. Lett.*, 79(1):26–30.

[Abele et al., 1997] Abele, H., Baessler, S., Dubbers, D., Last, J., Mayerhofer, U., Metz, C., Muller, T. M., Nesvizhevsky, V., Raven, C., Scharpf, O., et al. (1997). A measurement of the beta asymmetry a in the decay of free neutrons. *Phys. Lett. B*, 407(3-4):212–218.

[Abragam, 1961] Abragam, A. (1961). *The principles of nuclear magnetism*. Clarendon Press, Oxford, (Oxford, England).

[Ackerstaff et al., 1997] Ackerstaff, K., Airapetian, A., Akushevich, I., Akopov, N., Amarian, M., Aschenauer, E. C., Avakian, R., Avakian, H., Avetissian, A., Bains, B., et al. (1997). Measurement of the neutron spin structure function g_1^n with a polarized ^{3}He internal target. *Phys. Lett. B*, 404(3-4):383–389.

[Afnan and Birrell, 1977] Afnan, I. R. and Birrell, N. D. (1977). Comparison of unitary pole and Adhikari-Sloan expansions in 3–nucleon system. *Phys. Rev. C-Nucl. Phys.*, 16(2):823–838.

[Albert et al., 1994] Albert, M. S., Cates, G. D., Driehuys, B., Happer, W., Saam, B., Springer, C. S., and Wishnia, A. (1994). Biological magnetic-resonance-imaging using laser polarized ^{129}Xe. *Nature*, 370(6486):199–201.

[Altes et al., 1999] Altes, T. A., Powers, P. L., Knight-Scott, J., de Lange, E. E., Alford, B. A., and Brookeman, J. R. (1999). Asthma: Findings with hyperpolarized ^{3}He MR lung ventilation imaging. In *Abstracts of the 85th Annual Meeting of the Radiological Society of North America (RSNA)*.

[Alvarez, 1987] Alvarez, L. (1987). *Discovering Alvarez*. University of Chicago Press.

[Aminoff et al., 1989] Aminoff, C. G., Larat, C., Leduc, M., and Laloe, F. (1989). Optical-pumping of helium with arc lamp excited LNA lasers. *Revue. Phys. Appl.*, 24(8):827–831.

[Anderson and Ramsey, 1961] Anderson, L.W. and Ramsey, A. (1961). Effect of spin–excahnge collisions on the optical orientation of atomic sodium. *Phys. Rev.*, 124:1862.

[Anthony et al., 1996] Anthony, P. L., Arnold, R. G., Band, H. R., Borel, H., Bosted, P. E., Breton, V., Cates, G. D., Chupp, T. E., Dietrich, F. S., Dunne, J., et al. (1996). Deep inelastic scattering of polarized electrons by polarized ^{3}He and the study of the neutron spin structure. *Phys. Rev. D*, 54(11):6620–6650.

[Anthony et al., 1993] Anthony, P. L., Arnold, R. G., Band, H. R., Borel, H., et al. (1993). Determination of the neutron spin structure function. *Phys. Rev. Lett.*, 71:959–962.

[Appelt et al., 1998] Appelt, S., Baranga, A. B., Erickson, C. J., Romalis, M. V., Young, A. R., and Happer, W. (1998). Theory of spin-exchange optical pumping of ^{3}He and ^{129}Xe. *Phys. Rev. A*, 58(2):1412–1439.

[Appelt et al., 1995] Appelt, S., Wackerle, G., and Mehring, M. (1995). Geometric phase in nonadiabatic figure-8 experiments. *Phys. Lett. A*, 204(3-4):210–216.

[Arnett and Turan, 1985] Arnett, W. D. and Turan, J. W. (1985). *Nucleosynthesis*. University of Chicago Press.

[Bachert et al., 1996] Bachert, P., Schad, L. R., Bock, M., Knopp, M. V., Ebert, M., Grossmann, T., Heil, W., Hofmann, D., Surkau, R., and Otten, E. W. (1996). Nuclear magnetic resonance imaging of airways in humans with use of hyperpolarized ^{3}He. *Magn.Reson.Med.*, 36(2):192–196.

[Baranga et al., 1998] Baranga, A. B. A., Appelt, S., Romalis, M. V., Erickson, C. J., et al. (1998). Polarization of ^{3}He by spin exchange with optically pumped Rb and K vapors. *Phys. Rev. Lett.*, 80:2801–2804.

[Becker et al., 1998] Becker, J., Bermuth, J., Ebert, M., Grossmann, T., Heil, W., Hofmann, D., Humblot, H., Leduc, M., Otten, E. W., Rohe, D., et al. (1998). Interdisciplinary experiments with polarized ^{3}He. *Nucl. Instrum. Methods Phys. Res. Sect. A-Accel. Spectrom. Dect. Assoc. Equip.*, 402(2-3):327–336.

[Becker et al., 1994] Becker, J., Heil, W., Krug, B., Leduc, M., Meyerhoff, M., Nacher, P. J., Otten, E. W., Prokscha, T., Schearer, L. D., and Surkau, R. (1994). Study of mechanical compression of spin-polarized ^{3}He gas. *Nucl. Instrum. Methods Phys. Res. Sect. A-Accel. Spectrom. Dect. Assoc. Equip.*, 346(1-2):45–51.

[Bhaskar et al., 1982] Bhaskar, N. D., Happer, W., and McClelland, T. (1982). Efficiency of spin exchange between rubidium spins and ^{129}Xe nuclei in a gas. *Phys. Rev. Lett.*, 49(1):25–28.

[Bohler et al., 1988] Bohler, C. L., Schearer, L. D., Leduc, M., Nacher, P. J., Zachorowski, L., Milner, R. G., McKeown, R. D., and Woodward, C. E. (1988). Spin-polarized ^{3}He nuclear targets and metastable ^{4}He atoms by optical-pumping with a tunable, Nd-YAP laser. *J. Appl. Phys.*, 63(8):2497–2501.

[Bottomley et al., 1984] Bottomley, P. A., Foster, T. H., Argersinger, R. E., and Pfeifer, L. M. (1984). A review of normal tissue hydrogen NMR relaxation-times and relaxation mechanisms from 1-100 MHz - dependence on tissue- type, NMR frequency, temperature, species, excision, and age. *Med. Phys.*, 11(4):425–448.

[Bouchiat et al., 1972] Bouchiat, M. A., Brossel, J., and Pottier, L. C. (1972). Evidence for Rb–rare–gas molecules from the relaxation of polarized Rb atoms in a rare gas. experimental results. *J. Chem. Phys.*, 56:3703–3714.

[Bouchiat et al., 1960] Bouchiat, M. A., Carver, T. R., and Varnum, C. M. (1960). Nuclear polarization in ^{3}He gas induced by optical pumping and dipolar exchange. *Phys. Rev. Lett*, 5:373–375.

[Brookeman, 1998] Brookeman, J. (1998). MRS and MRI of hyperpolarized ^{129}Xe: Studies in human volunteers. In den Hollander, J., editor, *Advanced Spectroscopy*, pages 505–512. I.S.M.R.M.

[Calaprice et al., 1985] Calaprice, F. P., Happer, W., Schreiber, D. F., Lowry, M. M., Miron, E., and Zeng, X. (1985). Nuclear alignment and magnetic-moments of ^{133}Xe, ^{133}Xe^M, and ^{131}Xe^m by spin exchange with optically pumped Rb-87. *Phys. Rev. Lett.*, 54(3):174–177.

[Callaghan, 1991] Callaghan, P. T. (1991). *Principles of nuclear magnetic resonance microscopy*. Oxford University Press, Oxford, New York.

[Cates et al., 1990] Cates, G. D., Benton, D. R., Gatzke, M., Happer, W., Hasson, K. C., and Newbury, N. R. (1990). Laser production of large nuclear-spin polarization in frozen xenon. *Phys. Rev. Lett.*, 65(20):2591–2594.

[Cates et al., 1992] Cates, G. D., Fitzgerald, R. J., Barton, A. S., Bogorad, P., Gatzke, M., Newbury, N. R., and Saam, B. (1992). Rb ^{129}Xe spin-exchange rates due to binary and 3-body collisions at high xenon pressures. *Phys. Rev. A*, 45(7):4631–4639.

[Chawla et al., 1998] Chawla, M. S., Chen, X. J., Moller, H. E., Cofer, G. P., Wheeler, C. T., Hedlund, L. W., and Johnson, G. A. (1998). In vivo magnetic resonance vascular imaging using laser-polarized ^{3}He microbubbles. *Proc Natl Acad Sci U S A*, 95(18):10832–5.

[Che'en and Takeo, 1957] Che'en, S.-Y. and Takeo, M. (1957). Broadening and shift of spectral lines due to the presence of foreign gases. *Rev. Mod. Phys.*, 29:20–73.

[Chen et al., 1980] Chen, R., Fan, F., Kim, S., Jan, K., Usami, S., and Chien, S. (1980). Tissue-blood partition coefficients of xenon: temperature and hematocrit dependence. *J. Appl. Physiol.*, 49:179–181.

[Chen et al., 1998] Chen, X. J., Chawla, M. S., Cofer, G. P., Hedlund, L. W., Moller, H. E., and Johnson, G. A. (1998). Hyperpolarized ^{3}He NMR lineshape measurements in the live guinea pig lung. *Magn Reson Med*, 40(1):61–5.

[Cheron et al., 1995] Cheron, B., Gilles, H., Hamel, J., Leduc, M., Moreau, O., and Noel, E. (1995). ^{3}He nuclear-spin relaxation in cesium coated cells at room- temperature. *J. Phys. III*, 5(8):1287–1295.

[Chupp and Coulter, 1985] Chupp, T. E. and Coulter, K. P. (1985). Polarization of ^{3}He and ^{21}Ne by spin exchange with optically pumped Rb vapor. *Phys. Rev. Lett.*, 55(10):1074–1077.

[Chupp et al., 1987] Chupp, T. E., Wagshul, M. E., Coulter, K. P., McDonald, A. B., and Happer, W. (1987). Polarized, high-density, gaseous ^{3}He targets. *Phys. Rev. C-Nucl. Phys.*, 36(6):2244–2251.

[Chupp et al., 1988] Chupp, T. E., Oteiza, E. R., Richardson, J. M., and White, T. R. (1988). Precision frequency measurements with polarized ^{3}He, ^{21}Ne, and ^{129}Xe atoms. *Phys. Rev. A*, 38(8):3998–4003.

[Chupp et al., 1989] Chupp, T. E., Hoare, R. J., Loveman, R. A., Oteiza, E. R., Richardson, J. M., Wagshul, M. E., and Thompson, A. K. (1989). Results of a new test of local lorentz invariance - a search for mass anisotropy in ^{21}Ne. *Phys. Rev. Lett.*, 63(15):1541–1545.

[Chupp et al., 1992] Chupp, T. E., Loveman, R. A., Thompson, A. K., Bernstein, A. M., and Tieger, D. R. (1992). Tests of a high-density polarized ^{3}He target for electron- scattering. *Phys. Rev. C-Nucl. Phys.*, 45(3):915–930.

[Chupp et al., 1994a] Chupp, T. E., Holt, R. J., and Milner, R. G. (1994b). Optically pumped polarized H, D, and ^{3}He gas targets. *Annu. Rev. Nucl. Part. Sci.*, 44:373–411.

[Chupp et al., 1994b] Chupp, T. E., Hoare, R. J., Walsworth, R. L., and Wu, B. (1994a). Spin-exchange-pumped ^{3}He and ^{129}Xe zeeman masers. *Phys. Rev. Lett.*, 72(15):2363–2366.

[Chupp et al., 1996] Chupp, T. E., Coulter, K. P., Hwang, S. R., Smith, T., and Welsh, R. (1996). Progress toward a spin exchange pumped ^{3}He neutron spin filter. *Journal of Neutron Research*, 5:11–24.

[Colgrove et al., 1963] Colgrove, F. D., Schaerer, L. D., and Walters, G. K. (1963). Polarization of ^{3}He gas by optical pumping. *Phys. Rev.*, 132.

[Cosgrove and Mowat, 1974] Cosgrove, M. D. and Mowat, P. (1974). Evaluation of the ^{133}Xe renal blood flow method. *British Journal of Urology*, 46:134–47.

[Coulter et al., 1990] Coulter, K. P., Chupp, T. E., McDonald, A. B., Bowman, C. D., Bowman, J. D., Szymanski, J. J., Yuan, V., Cates, G. D., Benton, D. R., and Earle, E. D. (1990). Neutron polarization with a polarized ^{3}He spin filter. *Nucl. Instrum. Methods Phys. Res. Sect. A-Accel. Spectrom. Dect. Assoc. Equip.*, 288(2-3):463–466.

[Coulter et al., 1988] Coulter, K. P., McDonald, A. B., Happer, W., Chupp, T. E., and Wagshul, M. E. (1988). Neutron polarization with polarized ^{3}He. *Nucl. Instrum. Methods Phys. Res. Sect. A-Accel. Spectrom. Dect. Assoc. Equip.*, 270(1):90–94.

[Cremillieux et al., 1999] Cremillieux, Y., Berthezene, Y., Humblot, H., Viallon, M., Canet, E., Bourgeois, M., Albert, T., Heil, W., and Briguet, A. (1999). A combined ^{1}H perfusion/^{3}He ventilation NMR study in rat lungs. *Magn. Reson. Med.*, 41(4):645–648.

[Cummings et al., 1995] Cummings, W. J., Hausser, O., Lorenzon, W., Swenson, D. R., and Larson, B. (1995). Optical-pumping of Rb vapor using high-power Ga^{1-x}Al^{x}As diode–laser arrays. *Phys. Rev. A*, 51(6):4842–4851.

[Darrasse et al., 1998] Darrasse, L., Durand, E., Guillot, G., Nacher, P., and Tastevin, G. (1998). Fast spin echo imaging of hyperpolarized ^{3}He in human lungs at low field. *Magn. Res. Mat. in Phys, Biol. and Med.*, Suppl. 1 to Vol. 6:101.

[de Lange et al., 1999] de Lange, E. E., Mugler, J. P., Brookeman, J. R., Knight-Scott, J., Truwit, J. D., Teates, C. D., Daniel, T. M., Bogorad, P. L., and Cates, G. D. (1999). Lung air spaces: MR imaging evaluation with hyperpolarized ^{3}He gas. *Radiology*, 210(3):851–857.

[Driehuys et al., 1996] Driehuys, B., Cates, G. D., Miron, E., Sauer, K., Walter, D. K., and Happer, W. (1996). High-volume production of laser-polarized ^{129}Xe. *Appl. Phys. Lett.*, 69(12):1668–1670.

[Ebert et al., 1996] Ebert, M., Grossmann, T., Heil, W., Otten, W. E., Surkau, R., Leduc, M., Bachert, P., Knopp, M. V., Schad, L. R., and Thelen, M. (1996). Nuclear magnetic resonance imaging with hyperpolarised ^{3}He. *Lancet*, 347(9011):1297–1299.

[Edelstein et al., 1986] Edelstein, W. A., Glover, G. H., Hardy, C. J., and Redington, R. W. (1986). The intrinsic signal-to-noise ratio in NMR imaging. *Magn.Reson.Med.*, 3(4):604–618.

[Edelstein et al., 1980] Edelstein, W. A., Hutchison, J. M. S., Johnson, G., and Redpath, T. (1980). Spin warp NMR imaging and applications to human whole-body imaging. *Phys. Med. Biol.*, 25(4):751–756.

[Fitzsimmons and Sass, 1989] Fitzsimmons, M. R. and Sass, S. L. (1989). The atomic-structure of the twist boundary in gold determined using quantitative x-ray-diffraction techniques. *ACTA Metall.*, 37(4):1009.

[Fitzsimmons et al., 1969] Fitzsimmons, W. A., Tankersly, L. L., and Walters., G. K. (1969). Nature of surface–induced nuclear–spin relaxatoin of gaseous ^{3}He. *Phys. Rev.*, 179:156–165.

[Friar et al., 1990] Friar, J. L., Gibson, B. F., Payne, G. L., Bernstein, A. M., and Chupp, T. E. (1990). Neutron polarization in polarized ^{3}He targets. *Phys. Rev. C-Nucl. Phys.*, 42(6):2310–2314.

[Frossati, 1998] Frossati, G. (1998). Polarization of ^{3}He, D$_2$ (and possibly ^{129}Xe) using cryogenic techniques. *Nucl. Instrum. Methods Phys. Res. Sect. A-Accel. Spectrom. Dect. Assoc. Equip.*, 402(2-3):479–483.

[Gamblin and Carver, 1965] Gamblin, G. A. and Carver, T. R. (1965). Polarization and relaxation processes in ^{3}He gas. *Phys. Rev.*, 4:946–960.

[Gao, 1998] Gao, H. (1998). Precise measurement of the neutron magnetic form factor from quasielastic ^{3}He($\vec{e}, e'$)X. *Nucl. Instrum. Methods Phys. Res. Sect. A-Accel. Spectrom. Dect. Assoc. Equip.*, 402(2-3):277–283.

[Gatzke et al., 1993] Gatzke, M., Cates, G. D., Driehuys, B., Fox, D., Happer, W., and Saam, B. (1993). Extraordinarily slow nuclear-spin relaxation in frozen laser- polarized ^{129}Xe. *Phys. Rev. Lett.*, 70(5):690–693.

[Geen and Freeman, 1991] Geen, H. and Freeman, R. (1991). Band-selective radiofrequency pulses. *J. Magn. Reson.*, 93(1):93–141.

[Gentile et al., 1999] Gentile, T. R., Jones, G. L., Thompson, A. K., Rizi, R., Lipson, D., Roberts, D., Schnall, M., Brokeman, J., and III, J. M. (1999). A compact compressor for application of metastability–exchange optical pumping of ^{3}He to human lung imaging. *European Radiology*, 9:B17.

[Goldberg et al., 1998] Goldberg, L., Koplow, J. P., Moeller, R. P., and Kliner, D. A. V. (1998). High-power superfluorescent source with a side-pumped Yb-doped double-cladding fiber. *Opt. Lett.*, 23(13):1037–1039.

[Golub and Lamoreaux, 1994] Golub, R. and Lamoreaux, S. K. (1994). Neutron electric-dipole moment, ultracold neutrons and polarized ^{3}He. *Phys. Rep.-Rev. Sec. Phys. Lett.*, 237(1):1–62.

[Goodson, 1999] Goodson, B. M. (1999). Using injectable carriers of laser-polarized noble gases for enhancing NMR and MRI. *Concepts Magn. Resonance*, 11(4):203–223.

[Goodson et al., 1997] Goodson, B. M., Song, Y. Q., Taylor, R. E., Schepkin, V. D., Brennan, K. M., Chingas, G. C., Budinger, T. F., Navon, G., and Pines, A. (1997). In vivo NMR and MRI using injection delivery of laser-polarized xenon. *Proc. Natl. Acad. Sci. U. S. A.*, 94(26):14725–14729.

[Grover, 1983] Grover, B. (1983). Production of a nuclear–spin polarized ^{21}Ne sample. *Phys. Rev.*, A28:2521.

[Hagspiel et al., 1999] Hagspiel, K., Altes, T., III, J. M., Spellman, M., Mata, J., Tustison, N., Rudy, R., and Brookeman, J. (1999). MR virtual colonoscopy and hysterosalpingography using hyperpolarized ^{3}He as an endoluminal contrast agent. *European Radiology*, 9:B31.

[Hamel et al., 1987] Hamel, J., Cassimi, A., Abusafia, H., Leduc, M., and Schearer, L. D. (1987). Diode pumping of LNA lasers for helium optical-pumping. *Opt. Commun.*, 63(2):114–117.

[Happer, 1972] Happer, W. (1972). Optical pumping. *Rev. Mod. Phys.*, 44:169–249.

[Happer et al., 1984] Happer, W., Miron, E., Schaefer, S., Schreiber, D., Vanwijngaarden, W. A., and Zeng, X. (1984). Polarization of the nuclear spins of noble-gas atoms by spin exchange with optically pumped alkali-metal atoms. *Phys. Rev. A*, 29(6):3092–3110.

[Hasson et al., 1999a] Hasson, K., Bogorad, P., Driehuys, B., Kameya, G., Wheeler, B., and Zollinger, D. (1999a). Polarized ^{3}He production and transport system. *European Radiology*, 9:B16.

[Hasson et al., 1999b] Hasson, K., Cella, P., Deaton, D., Kameya, G., and Driehuys, B. (1999b). Continuous–flow production of polarized ^{129}Xe. *European Radiology*, 9:B10.

[Heckel et al., 1982] Heckel, B., Ramsey, N. F., Green, K., Greene, G. L., Gahler, R., Schaerpf, O., Forte, M., Dress, W., Miller, P. D., Golub, R., et al. (1982). A measurement of parity non-conserving neutron spin rotation in lead and tin. *Phys. Lett. B*, 119(4-6):298–302.

[Hedlund et al., 1999] Hedlund, L. W., Chawla, M. S., Chen, X. J., Cofer, G. P., Moller, H. E., and Johnson, G. A. (1999). MR microscopy in small animal models of pulmonary disease. *European Radiology*, 9:B32.

[Heil et al., 1998] Heil, W., Andersen, K., Hoffman, D., Humbolt, H., Kulda, J., Lelievre-Berna, E., Schärpf, O., and Tasset, F. (1998). ^{3}He neutron spin filter. *Physica*, B267-268:328–35.

[Herczeg, 1998] Herczeg, P. (1998). T-violation in semileptonic decays and CP-violation in extensions of the standard model *Particles Strings and Cosmology, ed. P. Nath.* World Scientific, Singapore:333-342.

[Herman, 1965] Herman, R. (1965). Theory of spin exchange between optically pumped rb and foreign gas nuclei. *Phys. Rev. A*, 137:10621065.

[Himbert et al., 1989] Himbert, M., Dupontroc, J., and Lhuillier, C. (1989). Spin-diffusion coefficient in gaseous helium between 1-k and 0.5-k. *Phys. Rev. A*, 39(12):6170–6177.

[Holstein, 1947] Holstein, T. (1947). Imprisonment of resonance radiation in gases. *Phys. Rev.*, 72:1212–1233.

[Hrycyshyn and Krause, 1970] Hrycyshyn and Krause, L. (1970). Inelastic collisions between excited alkali atoms and molecules. Sensitized fluorescence and quenching in mixtures of rubidium with H-2, HD, D$_2$, N$_2$, CD$_4$, C$_2$H$_4$, and C$_2$H$_6$. *Can. J. Phys.*, 48(22):2761.

[Hunt and Carr, 1963] Hunt, E. R. and Carr, H. Y. (1963). Nuclear magnetic resonance of ^{129}Xe in natural xenon. *Phys. Rev.*, 130:2302.

[Jackson et al., 1957] D.Jackson, J., B.Trieman, S., and Wyld, H. W. (1957). Possible tests of time reversal invariance in beta decay. *Phys. Rev.*, 106:517–521.

[Jameson et al., 1988] Jameson, C. J., Jameson, A. K., and Hwang, J. K. (1988). Nuclear-spin relaxation by intermolecular magnetic dipole coupling in the gas–phase ^{129}Xe in oxygen. *J. Chem. Phys.*, 89(7):4074–4081.

[Kadlecek et al., 1998] Kadlecek, S., Anderson, L., and Walker, T. (1998). Field dependence of spin relaxation in a dense Rb vapor. *Phys. Rev. Lett.*, 80:5512.

[Kastler, 1950] Kastler, W. A. J. (1950). Some suggestions concerning the production and detection by optical means of inequalities in populations of levels of spatial quantization in atoms. *J. Phys. Radium*, 11:225.

[Kauczor et al., 1997] Kauczor, H. U., Ebert, M., Kreitner, K. F., Nilgens, H., Surkau, R., Heil, W., Hofmann, D., Otten, E. W., and Thelen, M. (1997). Imaging of the lungs using ^{3}He MRI: Preliminary clinical experience in 18 patients with and without lung disease. *JMRI-J. Magn. Reson. Imaging*, 7(3):538–543.

[Kauczor et al., 1998] Kauczor, H. U., Surkau, R., and Roberts, T. (1998). MRI using hyperpolarized noble gases. *Eur. Radiol.*, 8(5):820–827.

[Kety and Schmidt, 1945] Kety, S. and Schmidt, C. F. (1945). The determination of cerebral blood flow in man by the use of nitrous oxide in low concentrations. *Am. J. Physiol.*, 143:53–66.

[Kubler, 1981] Kubler, J. (1981). Magnetic-moments of ferromagnetic and anti-ferromagnetic BCC and FCC iron. *Phys. Lett. A*, 81(1):81–83.

[Kumar et al., 1975] Kumar, A., Welti, D., and Ernst, R. R. (1975). NMR fourier zeugmatography. *J. Magn. Reson.*, 18(1):69–83.

[Larson and et al., 1991] Larson, B. and et al. (1991). Optical pumping of Rb in the presence of high-pressure ^{3}He buffer gas. *Phys. Rev.*, A44:3108.

[Lassen, 1980] Lassen, N. (1980). *Cerebral blood flow determined by radioactive diffusible tracers with special regard to the use of Xenon-133 in Cerebral Metabolism and Neural Function*. Williams and Wilkins.

[Lassen and Ingvar, 1961] Lassen, N. and Ingvar, D. (1961). The blood flow of the cerebral cortex determined by radioactive krypton-85. *Experientia*, 17:42.

[Lauterbur, 1973] Lauterbur, P. C. (1973). Image formation by induced local interactions - examples employing nuclear magnetic resonance. *Nature*, 242(5394):190–1.

[Leduc et al., 1987] Leduc, M., Nacher, P. J., Betts, D. S., Daniels, J. M., Tastevin, G., and Laloe, F. (1987). Nuclear-polarization and heat-conduction changes in gaseous ^{3}He. *Europhys. Lett.*, 4(1):59–64.

[Lee et al., 1999] Lee, J. H., Ryu, U. C., and Park, N. (1999). Passive erbium-doped fiber seed photon generator for high-power Er3$^+$–doped fiber fluorescent sources with an 80-nm bandwidth. *Opt. Lett.*, 24(5):279–281.

[Lefevre-Seguin and Leduc, 1977] Lefevre-Seguin, V. and Leduc, M. (1977). Metastability-exchange and depolarizing collisions in xenon and krypton. *J. Phys. B-At. Mol. Opt. Phys.*, 10(11):2157–2164.

[Lorenzon et al., 1993] Lorenzon, W., Gentile, T. R., Gao, H., and McKeown, R. D. (1993). NMR calibration of optical measurement of nuclear-polarization in ^{3}He. *Phys. Rev. A*, 47(1):468–479.

[Lounasmaa, 1974] Lounasmaa, O. V. (1974). *Experimental principles and methods below 1 K*. Academic Press, London ; New York.

[MacAdam et al., 1992] MacAdam, K. B., Steinbach, A., and Wieman, C. (1992). A narrow-band tunable diode laser system with grating feedback and a saturated absorption spectrometer for Cs and Rb. *Am. J. Phys.*, 60:1098.

[Mair et al., 1999] Mair, R. W., Wong, G. P., Hoffmann, D., Hurlimann, M. D., Patz, S., Schwartz, L. M., and Walsworth, R. L. (1999). Probing porous media with gas diffusion NMR. *Phys. Rev. Lett.*, 83(16):3324–3327.

[Mansfield and Grannell, 1973] Mansfield, P. and Grannell, P. (1973). NMR diffraction in solids. *J. Phys. C*, 6(22):L422–L426.

[Marcus et al., 1987] Marcus, M. L., Wilson, R. F., and White, C. W. (1987). Methods of measurement of myocardial blood flow in patients: a critical review. *Circulation*, 76:245–53.

[Martin et al., 1997] Martin, C. C., Williams, R. F., Gao, J. H., Nickerson, L. D., Xiong, J., and Fox, P. T. (1997). The pharmacokinetics of hyperpolarized xenon: implications for cerebral MRI. *J Magn Reson Imaging*, 7(5):848–54.

[Middleton et al., 1995] Middleton, H., Black, R. D., Saam, B., Cates, G. D., Cofer, G. P., Guenther, R., Happer, W., Hedlund, L. W., Johnson, G. A., Juvan, K., et al. (1995). MR-imaging with hyperpolarized ^{3}He gas. *Magn.Reson.Med.*, 33(2):271–275.

[Middleton et al., 1993] Middleton, H., Cates, G. D., Chupp, T. E., Driehuys, B., Hughes, E. W., Johnson, J. R., Meyer, W., Newbury, N. R., Smith, T. B., and Thompson, A. (1993). The SLAC high–density ^{3}He target polarized by spin–exchange optical pumping, volume 293. *AIP Conference Proceedings*.

[Mitchell et al., 1999] Mitchell, G. E., Bowman, J. D., and Weidenmuller, H. A. (1999). Parity violation in the compound nucleus. *Rev. Mod. Phys.*, 71(1):445–457.

[Moller et al., 1999a] Moller, H. E., Chawla, M. S., Chen, X. J., Driehuys, B., Hedlund, L. W., Wheeler, C. T., and Johnson, G. A. (1999a). Magnetic resonance angiography with hyperpolarized ^{129}Xe dissolved in a lipid emulsion. *Magn. Reson. Med.*, 41(5):1058–1064.

[Moller et al., 1999b] Moller, H. E., Chen, X. J., Chawla, M. S., Cofer, G. P., Driehuys, B., Hedlund, L. W., Suddarth, S. A., and Johnson, G. A. (1999b). Sensitivity and resolution in 3–D NMR microscopy of the lung with hyperpolarized noble gases. *Magn Reson Med*, 41(4):800–8.

[Mugler et al., 1997] Mugler, J. P., Driehuys, B., Brookeman, J. R., Cates, G. D., Berr, S. S., Bryant, R. G., Daniel, T. M., deLange, E. E., Downs, J. H., Erickson, C. J., et al. (1997). MR imaging and spectroscopy using hyperpolarized ^{129}Xe gas: Preliminary human results. *Magn.Reson.Med.*, 37(6):809–815.

[Mullin et al., 1990] Mullin, W. J., Laloe, F., and Richards, M. G. (1990). Longitudinal relaxation-time for dilute quantum gases. *J. Low Temp. Phys.*, 80(1-2):1–13.

[Nacher and Stolz, 1995] Nacher, P. and Stolz, E. (1995). NMR studies of highly polarized liquid ^{3}He–^{4}He mixtures. *J. Low Temp. Phys.*, 101:6170–6177.

[Nacher and Leduc, 1985] Nacher, P. J. and Leduc, M. (1985). Optical pumping in ^{3}He with a laser. *J. de Physique*, 46(12):2057–2073.

[Nelson et al., 1999] Nelson, I., Chann, B., and Walker, T. (1999). Spin–exchange optical pumping using a frequency–narrowed high power diode laser. *submitted*.

[Newbury et al., 1993] Newbury, N. R., Barton, A. S., Cates, G. D., Happer, W., and Middleton, H. (1993). Gaseous ^{3}He–^{3}He magnetic dipolar spin relaxation. *Phys. Rev. A*, 48(6):4411–4420.

[Ogawa et al., 1990] Ogawa, S., Lee, T. M., Kay, A. R., and Tank, D. W. (1990). Brain magnetic-resonance-imaging with contrast dependent on blood oxygenation. *Proc. Natl. Acad. Sci. U. S. A.*, 87(24):9868–9872.

[Oteiza, 1992] Oteiza, E. R. (1992). *Search for a permanent electronic dipole moment in ^{129}Xe using simultaneous ^{3}He magnetometry*. PhD thesis, Harvard University.

[Peled et al., 1996] Peled, S., Jolesz, F. A., Tseng, C. H., Nascimben, L., Albert, M. S., and Walsworth, R. L. (1996). Determinants of tissue delivery for ^{129}Xe magnetic resonance in humans. *Magn.Reson.Med.*, 36(3):340–344.

[Peled et al., 1999] Peled, S., Tseng, C. H., Sodickson, A. A., Mair, R. W., Walsworth, R. L., and Cory, D. G. (1999). Single-shot diffusion measurement in laser-polarized gas. *J. Magn. Reson.*, 140(2):320–324.

[Phelps, 1991] Phelps, M. E. (1991). PET – a biological imaging technique. *Neurochem. Res.*, 16(9):929–940.

[Raftery et al., 1991] Raftery, D., Long, H., Meersmann, T., Grandinetti, P. J., Reven, L., and Pines, A. (1991). High-field NMR of adsorbed xenon polarized by laser pumping. *Phys. Rev. Lett.*, 66(5):584–587.

[Ramsey, 1953] Ramsey, N. (1953). *Nuclear moments*. Wiley, New York.

[Richards et al., 1988] Richards, M. G., Cowan, B. P., Secca, M. F., and Machin, K. (1988). The ^{3}He nuclear zeeman maser. *J. Phys. B-At. Mol. Opt. Phys.*, 21(4):665–681.

[Rizi et al., 1998] Rizi, R. R., Dimitrov, I. E., Thompson, A., Jones, G., Gentile, T. R., Ishii, M., Reddy, R., Schnall, M. D., and Leigh, J. S. (1998). MRI of hyperpolarized ^{3}He gas in human paranasal sinuses. *Magn. Reson. Med.*, 39(6):865–868.

[Robinson and Myint, 1964] Robinson, H. and Myint, T. (1964). ^{3}He nuclear zeeman maser. *Applied Phys. Lett.*, 5:116.

[Romalis et al., 1998] Romalis, M. V., Bogorad, P. L., Cates, G. D., Chupp, T. E., Coulter, K. P., Hughes, E. W., Johnson, J. R., Kumar, K. S., Smith, T. B., Thompson, A. K., et al. (1998). Toward precision polarimetry of dense polarized ^{3}He targets. *Nucl. Instrum. Methods Phys. Res. Sect. A-Accel. Spectrom. Dect. Assoc. Equip.*, 402(2-3):260–267.

[Rosen et al., 1999] Rosen, M. S., Chupp, T. E., Coulter, K. P., Welsh, R. C., and Swanson, S. D. (1999). Polarized ^{129}Xe optical pumping/spin exchange and delivery system for magnetic resonance spectroscopy and imaging studies. *Rev. Sci. Instrum.*, 70(2):1546–1552.

[Rosenberry, 1999] Rosenberry, M. A. (1999). *A precision measurement of the ^{129}Xe electric dipole moment using dual noble gas masers*. PhD thesis, University of Michigan.

[Saam et al., 1996] Saam, B., Drukker, N., and Happer, W. (1996). Edge enhancement observed with hyperpolarized ^{3}He. *Chem. Phys. Lett.*, 263(3-4):481–487.

[Saam et al., 1999] Saam, B., Yablonskiy, D. A., Gierada, D. S., and Conradi, M. S. (1996). Rapid imaging of hyperpolarized gas using EPI. *Mag. Reon. Med.*, 42:507–514.

[Sakai et al., 1996] Sakai, K., Bilek, A. M., Oteiza, E., Walsworth, R. L., Balamore, D., Jolesz, F. A., and Albert, M. S. (1996). Temporal dynamics of hyperpolarized ^{129}Xe resonances in living rats. *J. Magn. Reson. Ser. B*, 111(3):300–304.

[Sauer et al., 1999] Sauer, K. L., Fitzgerald, R. J., and Happer, W. (1999). Resonance technique to probe ^{129}Xe surface interactions. *Phys. Rev. A*, 59(3):R1746–R1749.

[Schaerer, 1969] Schaerer, L. D. (1969). Optical pumping of $^3P_2$ argon and xenon atoms. *Phys. Lett.*, 28A:660–661.

[Schearer and Leduc, 1986] Schearer, L. and Leduc, M. (1986). Tuning characteristics and new laser lines in an Nd-YAP CW laser. *IEEE J. Quantum Electron.*, 22(6):756–758.

[Shulman et al., 1993] Shulman, R., Blaimire, A., Rothman, D., and McCarthy, G. (1993). Nuclear magnetic resonance imaging and spectroscopy of human brain function. *Proc. Natl. Acad. Sci. U.S.A.*, 90:3127.

[Smith, 1998] Smith, T. B. (1998). *A precision measurement of the neutron spin structure functions using a polarized ^{3}He target*. PhD thesis, University of Michigan.

[Song et al., 1999] Song, Y. Q., Goodson, B. M., and Pines, A. (1999). NMR and MRI using laser–polarized xenon. *Spectroscopy*, 14:26–33.

[Song et al., 1998] Song, Y. Q., Goodson, B. M., Sheridan, B., de Swiet, T. M., and Pines, A. (1998). Effects of diffusion on magnetic resonance imaging of laser- polarized xenon gas. *J. Chem. Phys.*, 108(15):6233–6239.

[Stoner et al., 1996] Stoner, R. E., Rosenberry, M. A., Wright, J. T., Chupp, T. E., Oteiza, E. R., and Walsworth, R. L. (1996). Demonstration of a two species noble gas maser. *Phys. Rev. Lett.*, 77(19):3971–3974.

[Surkau et al., 1997] Surkau, R., Becker, J., Ebert, M., Grossmann, T., Heil, W., Hofmann, D., Humblot, H., Leduc, M., Otten, E. W., Rohe, D., et al. (1997). Realization of a broad band neutron spin filter with compressed, polarized ^{3}He gas. *Nucl. Instrum. Methods Phys. Res. Sect. A-Accel. Spectrom. Dect. Assoc. Equip.*, 384(2-3):444–450.

[Surkau et al., 1999] Surkau, R., Denninger, A., Bermuth, J., Ebert, M., Grossmann, T., Heil, W., Lauer, L., Otten, E., and Schmiedeskamp, J. (1999). Highly polarized ^{3}He for lung–MRI. *European Radiology*, 9:B15.

[Swanson et al., 1999a] Swanson, S. D., Chupp, T. E., Coulter, K. P., and Rosen, M. S. (1999a). Tissue perfusion using laser–polarized ^{129}Xe. *European Radiology*, 9:B40.

[Swanson et al., 1997] Swanson, S. D., Rosen, M. S., Agranoff, B. W., Coulter, K. P., Welsh, R. C., and Chupp, T. E. (1997). Brain MRI with laser-polarized ^{129}Xe. *Magn.Reson.Med.*, 38(5):695–698.

[Swanson et al., 1999b] Swanson, S. D., Rosen, M. S., Coulter, K. P., Welsh, R. C., and Chupp, T. E. (1999b). Distribution and dynamics of laser-polarized ^{129}Xe magnetization in vivo. *Magn. Reson. Med.*, 42(6):1137–1145.

[Tastevin et al., 1985] Tastevin, G., Nacher, P. J., Leduc, M., and Laloe, F. (1985). Direct detection of spin-waves in gaseous ^{3}He. *J. de Physique Lett.*, 46(6):L249–L254.

[Thompson et al., 1992] Thompson, A. K., Bernstein, A. M., Chupp, T. E., Deangelis, D. J., Dodge, G. E., Dodson, G., Dow, K. A., Farkhondeh, M., Fong, W., Kim, J. Y., et al. (1992). Quasi-elastic scattering of polarized electrons from polarized ^{3}He and measurement of the neutrons form-factors. *Phys. Rev. Lett.*, 68(19):2901–2904.

[Timsit et al., 1971a] Timsit, R. S., Daniels, J. M., Denning, E. I., Kiang, A. K. C., and May, A. D. (1971a). An experiment to compress polarized ^{3}He gas. *Can. J. Phys.*, 49:508.

[Timsit et al., 1971b] Timsit, R. S., Daniels, J. M., and May, A. D. (1971b). Nuclear relaxation of ^{3}He gas on various solid surfaces. *Can. J. Phys.*, 49(5):560.

[Trimble, 1982] Trimble, V. (1982). Super-novae *Rev. Mod. Phys.*, 54(4):1183–1224.

[Tseng et al., 1998] Tseng, C. H., Wong, G. P., Pomeroy, V. R., Mair, R. W., Hinton, D. P., Hoffmann, D., Stoner, R. E., Hersman, F. W., Cory, D. G., and Walsworth, R. L. (1998). Low-field MRI of laser polarized noble gas. *Phys. Rev. Lett.*, 81(17):3785–3788.

[Viallon et al., 1999] Viallon, M., Cofer, G. P., Suddarth, S. A., Moller, H. E., Chen, X. J., Chawla, M. S., Hedlund, L. W., Cremillieux, Y., and Johnson, G. A. (1999). Functional MR microscopy of the lung using hyperpolarized ^{3}He. *Magn Reson Med*, 41(4):787–92.

[Wagshul and Chupp, 1989] Wagshul, M. and Chupp, T. (1989). Optical–pumping of high–density Rb with a broad–band dye–laser and GaAlAs diode–laser arrays: Application to ^{3}He polarization. *Phys. Rev.*, A24:827.

[Wagshul et al., 1996] Wagshul, M. E., Button, T. M., Li, H. F. F., Liang, Z. R., Springer, C. S., Zhong, K., and Wishnia, A. (1996). In vivo MR imaging and spectroscopy using hyperpolarized ^{129}Xe. *Magn. Reson. Med.*, 36:183–191.

[Wagshul and Chupp, 1994] Wagshul, M. E. and Chupp, T. E. (1994). Laser optical-pumping of high-density Rb in polarized ^{3}He targets. *Phys. Rev. A*, 49:3854–3869.

[Walker, 1989] Walker, T. G. (1989). Estimates of spin-exchange parameters for alkali-metal noble–gas pairs. *Phys. Rev. A*, 40(9):4959–4963.

[Walker and Happer, 1997] Walker, T. G. and Happer, W. (1997). Spin-exchange optical pumping of noble-gas nuclei. *Rev. Mod. Phys.*, 69(2):629–642.

[Wehrli, 1995] Wehrli, F. W. (1995). From NMR diffraction and zeugmatography to modern imaging and beyond. *Prog. Nucl. Magn. Reson. Spectrosc.*, 28:87–135.

[Welsh et al., 1998] Welsh, R. C., Chupp, T. E., Coulter, K. P., Rosen, M. S., and Swanson, S. D. (1998). Magnetic resonance imaging with laser-polarized ^{129}Xe. *Nucl. Instrum. Methods Phys. Res. Sect. A-Accel. Spectrom. Dect. Assoc. Equip.*, 402(2-3):461–463.

[Williams, 1980] Williams, W. G. (1980). Neutron polarizers. *Nukleonika*, 25:769–786.

[Wilson et al., 1999] Wilson, G. J., Santyr, G. E., Anderson, M. E., and DeLuca, P. M. (1999). Longitudinal relaxation times of ^{129}Xe in rat tissue homogenates at 9.4 T. *Magn. Reson. Med.*, 41(5):933–938.

[Wittenberg et al., 1986] Wittenberg, L. J., Santarius, J. F., and Kulcinski, G. L. (1986). Lunar source of ^{3}He for commercial fusion power. *Fusion Technol.*, 10(2):167–178.

[Wolber et al., 1999a] Wolber, J., Cherubini, A., Dzik-Jurasz, A., Leach, M., and Bifone, A. (1999a). Spin-lattice relaxation of laser-polarized xenon in human blood. *Proc. Natl. Acad. Sci. U. S. A.*, 96(7):3664–3669.

[Wolber et al., 1999b] Wolber, J., Cherubini, A., Leach, M., and Bifone, A. (1999b). Hyperpolarized ^{129}Xe as a sensitive NMR probe for blood oxygenation. *European Radiology*, 9:B42.

[Wolber et al., 1998] Wolber, J., Rowland, I. J., Leach, M. O., and Bifone, A. (1998). Intravascular delivery of hyperpolarized ^{129}Xe for in vivo MRI. *Appl. Magn. Reson.*, 15(3-4):343–352.

[Woodward et al., 1990] Woodward, C. E., Beise, E. J., Belz, J. E., Carr, R. W., Filippone, B. W., Lorenzon, W. B., McKeown, R. D., Mueller, B., Oneill, T. G., Dodson, G., et al. (1990). Measurement of inclusive quasi-elastic scattering of polarized electrons from polarized ^{3}He. *Phys. Rev. Lett.*, 65(6):698–700.

[Zeng et al., 1985] Zeng, X., Wu, Z., Call, T., Miron, E., Schreiber, D., and Happer, W. (1985). Experimental-determination of the rate constants for spin exchange between optically pumped K, Rb, and Cs atoms and ^{129}Xe nuclei in alkali-metal noble-gas Van der Waals molecules. *Phys. Rev. A*, 31(1):260–278.

[Zerger et al., 1999] Zerger, J., Lim, M., Coulter, K., and Chupp, T. (1999). Polarization of ^{129}Xe with high power external–cavity laser diode arrays. *submitted to Appl. Phys. Lett.*

[Zhao et al., 1996] L.Zhao, Mulkern, R., Tseng, C., WIlliamson, D., Patz, S., Kraft, R., Walsworth, R., Jolez, F., and Albert, M. (1996). Pulse sequence considerations for biomedical imaging with hyperpolarized noble gas MRI. *J. Mag. Res.*, 113:179.